

Formin3 directs dendritic architecture via microtubule regulation and is required for somatosensory nociceptive behavior

Keywords: dendrite, Formin3, microtubule, INF2, nociception, CMT

Ravi Das^{1,†}, Shatabdi Bhattacharjee^{1,†}, Jamin M. Letcher^{1,†}, Jenna M. Harris¹, Sumit Nanda², Istvan Foldi³, Erin N. Lottes¹, Hansley M. Bobo¹, Benjamin D. Grantier¹, József Mihály³, Giorgio A. Ascoli², Daniel N. Cox^{1,*}.

¹Neuroscience Institute, Georgia State University, Atlanta, GA, 30303, USA

²Krasnow Institute for Advanced Study, George Mason University, Fairfax, VA, 22030, USA

³Biological Research Centre, Hungarian Academy of Sciences, Institute of Genetics, MTA SZBK NAP B Axon Growth and Regeneration Group, Temesvári krt. 62, Szeged, H-6726, Hungary

†These authors contributed equally to this work

***Corresponding Author:** Daniel N. Cox

Neuroscience Institute
Georgia State University
P.O. Box 5030
Atlanta, GA 30302-5030
Phone: 404-413-5222
FAX: 404-413-5446
E-mail: dcox18@gsu.edu

Conflict of Interest: The authors declare no competing financial interests

Acknowledgements:

This research was supported by NIH R01 NS086082 (DNC/GAA); NIH R01 NS115209 (DNC); R01 NS39600 (GAA); NSF BRAIN EAGER DBI-1546335 (GAA); Hungarian Brain Research Program (KTIA_NAP_13-2-2014-0007; 2017-1.2.1-NKP-2017-00002) (JM), the National Research, Development and Innovation Office (GINOP-2.3.2-15-2016-00032) (JM) and the OKTA Postdoctoral Fellowship (PD 128357) (IF). We gratefully acknowledge Drs. Akinao Nose, Yuh-Nung Jan, Daniel P. Kiehart, Chris Q. Doe, and W. Daniel Tracey for reagents and fly strains. We thank the Bloomington *Drosophila* Stock Center (NIH P40ODO18537) and Vienna *Drosophila* Resource Center (VDRC) for fly strains used in this study.

Abstract

Dendrite shape impacts functional connectivity and is mediated by organization and dynamics of cytoskeletal fibers. Identifying molecular factors that regulate dendritic cytoskeletal architecture is therefore important in understanding mechanistic links between cytoskeletal organization and neuronal function. We identified Formin3 (Form3) as a critical regulator of cytoskeletal architecture in

nociceptive sensory neurons in *Drosophila* larvae. Time course analyses reveal Form3 is cell-autonomously required to promote dendritic arbor complexity. We show that *form3* is required for the maintenance of a population of stable dendritic microtubules (MTs), and mutants exhibit defects in the localization of dendritic mitochondria, satellite Golgi, and the TRPA channel Painless. Form3 directly interacts with MTs via FH1-FH2 domains. Mutations in human Inverted Formin 2 (*INF2*; ortholog of *form3*) have been causally linked to Charcot-Marie-Tooth (CMT) disease. CMT sensory neuropathies lead to impaired peripheral sensitivity. Defects in *form3* function in nociceptive neurons result in severe impairment of noxious heat-evoked behaviors. Expression of the INF2 FH1-FH2 domains partially recovers *form3* defects in MTs and nocifensive behavior, suggesting conserved functions, thereby providing putative mechanistic insights into potential etiologies of CMT sensory neuropathies.

Introduction

Dendrites function in the reception, integration, and propagation of sensory or synaptic information and thereby mediate neural computation. Specification and maturation of diverse dendritic architectures is subject to complex intrinsic and extrinsic regulatory programs that modulate the formation and plasticity of a functional nervous system (Lefebvre *et al.* 2015). An important convergent regulatory target of extrinsic signaling and intrinsic factors is modulation of the neuronal cytoskeleton, which ultimately contributes to dendritic form and function (Das *et al.* 2017; Nanda *et al.* 2017). Thus, elucidating molecular bases underlying dendritic cytoskeletal organization is crucial to uncovering principles governing neuronal diversity, as well as potential mechanistic links between architecture and behavior.

Regulation of the cytoskeleton is important to the establishment, maintenance, and plasticity of neural morphology, as well as function (Franker and Hoogenraad 2013). Upon achieving a mature shape, dendritic arbors retain a certain degree of plasticity that occurs via dynamic cytoskeletal modulation, thereby contributing to refinements in neural connectivity. Moreover, stabilization of

mature dendrites is required for proper function, as morphological destabilization can lead to functional impairments in neurotransmission, result in neurodegeneration, disrupt organelle trafficking, and in the case of sensory neurons, disrupt responses to environmental stimuli, leading to behavioral defects such as peripheral insensitivity (Nanda *et al.* 2017; Honjo *et al.* 2016). Architectural organization and dynamic modulation of cytoskeletal fibers is controlled by a vast array of regulatory factors that impact assembly, disassembly, bundling, severing, stabilization, and motor-based transport (Coles and Bradke 2015; Kapitein and Hoogenraad 2015). In addition, defects in cytoskeletal-mediated motor-based transport result in loss of dendritic identity, defects in neuronal polarity, and severe impairments in dendritic development (Rolls 2011; Nanda *et al.* 2017).

Formins represent one important family of evolutionarily conserved, multi-functional cytoskeletal regulators (Goode and Eck 2007). Formins are multidomain, dimeric functional molecules characterized by conserved Formin Homology (FH) domains (Higgs 2005). The functional role of Formins in actin polymerization has been well documented, wherein the FH2 domain initiates actin nucleation and remains bound at the barbed end of an F-actin filament, moving along the growing filament and promoting elongation by preventing access of capping proteins (Chhabra and Higgs 2007). F-actin elongation is further enhanced by association of Profilin with the Formin FH1 domain (Kovar 2006). Unlike other actin nucleators, such as Arp2/3, that form branched actin filaments, Formins assemble linear actin filaments (Evangelista *et al.* 2002). Despite their basic function and properties, Formins vary significantly; for instance, some bundle actin filaments, some sever or depolymerize actin filaments, and in recent studies, Formins have been implicated in regulating microtubule (MT) organization and dynamics (Bartolini and Gundersen 2010; Breitsprecher and Goode 2013; Roth-Johnson *et al.* 2014). Formins appear to stabilize MTs both through their direct binding and/or by altering their post-translational state (Gaillard *et al.* 2011; Thurston *et al.* 2012). Recent studies have begun to elucidate roles of Formins in neural development, including dendrite morphogenesis (Galbraith

and Kengaku, 2019), however much remains unknown regarding mechanistic roles of Formins in dendritic arborization.

Here, we provide mechanistic links between Formin-mediated dendritic cytoskeletal regulation and nociceptive behavioral sensitivity. Specifically, we demonstrate that Formin3 (Form3) is required for dendritic arbor growth, with a major role in regulating a population of stable dendritic MTs. Moreover, *form3* mutants exhibit defects in dendritic localization of mitochondria and satellite Golgi. Biochemical analyses further reveal Form3 directly interacts with MTs via FH1-FH2 domains. Intriguingly, defects in *INF2* have been causally linked to CMT sensory neuropathies known to cause impaired peripheral sensitivity. Disruption of *form3* in nociceptive neurons severely impairs noxious heat-evoked behaviors and leads to mislocalization of the TRPA channel Painless. Moreover, *form3* mutant defects in nociceptive behavioral sensitivity and reductions in stable dendritic MTs can be partially recovered by expression of INF2 FH1-FH2 domains. Collectively, our findings suggest *form3* and *INF2* have conserved functions that may provide mechanistic insights into potential etiologies underlying CMT sensory neuropathies.

Materials and methods

Drosophila husbandry and stocks

Drosophila stocks were maintained at 25°C, and genetic crosses were performed at 29°C. Age-matched wandering third instar larvae of both sexes were used for all experiments. The following stocks were used in this study, where ‘B’ represents stocks from Bloomington Stock Center, ‘v’ represents those from Vienna Stock center, and additional sources are provided parenthetically: *GAL4⁴⁷⁷, UAS-mCD8::GFP/CyO, tubP-GAL80; GAL4^{ppk.1.9}, UAS-mCD8::GFP (CIV-GAL4); GAL4⁴⁷⁷, UASmCD8::GFP (CIV-GAL4); GAL4⁴⁷⁷; ppk::tdTomato; UAS-GMA::GFP; GAL4⁴⁷⁷, UAS-Jupiter::mCherry (Das *et al.* 2017); UAS-*form3*-B1 (Tanaka *et al.* 2004); *form3^{Em41}, FRT^{2A}* (missense: A376>V) (Tanaka *et al.* 2004; this study); *form3^{Em31}, FRT^{2A}* (nonsense: R428>Stop) (Tanaka *et al.* 2004; this study); *GAL4⁵⁻⁴⁰, UAS-**

Venus, *SOP-FLP⁴²*; +; *tubP-GAL80,FRT^{2A}* (DGRC stock 109-950); *GAL4^{Nanos}*; +; *form3-IR/ppk::tdTomato* (B7303; this study); *UAS-mito-HA-GFP.AP* (B8442); *UAS-manII::EGFP*; *GAL4^{ppk}*, *UAS-myr::GFP*; *UAS-INF2-FH1-FH2*; *UAS-INF2-Full length*; *UAS-Painless^{p103}::VFP* (Hwang *et al.* 2012); *UAS-capu-IR* (B2922); *UAS-dia-IR* (B33424, B35479); *UAS-Fhos-IR* (B31400, B51391); *UAS-Frl-IR* (B32447, v110438); *UAS-DAAM-IR* (B39058); *UAS-form3-IR* (B32398; focus of analyses in this study; v45594; v42302; v28437; v107473); and *UASp-alphaTub84B.tdEOS* (B51314). *OregonR* (*ORR*) or *w¹¹¹⁸* were used as a control strain for genetic outcrosses. The UP-TORR Fly website (<https://www.flyrnai.org/up-torr/>) was used to computationally evaluate putative off-target effects for *UAS-form3-IR* transgenes used in this study and stock B32398 targets both *form3* isoforms with zero predicted off-target effects in the fly genome.

IHC analysis, live confocal imaging and antibody generation

Larval filets were processed and labeled as previously described (Sulkowski *et al.* 2011). Primary antibodies used in this study include: rabbit anti-Form3 (1:100; this study), mouse anti-Futsch (1:200; DSHB catalog #22C10), anti-HRP (1:200; Jackson Immunoresearch catalog #123-475-021), and chicken anti-GFP (1:1000; Abcam catalog #ab13970). Donkey anti-rabbit, anti-mouse and anti-chicken secondary antibodies (Jackson Immunoresearch) were used at 1:200. IHC slides were then mounted in Fluoromount Aqueous Mounting Medium (Sigma), and imaged at room temperature on a Zeiss LSM780 confocal system with either a 20× Plan Apo, 0.8 NA (dry), 40× Plan Apo, 1.4 NA (oil) or 60× Plan Apo, 1.4 NA (oil) objective. Zen blue software was used to quantify the mean intensity of the fluorescence. Live confocal imaging was performed as described (Iyer *et al.* 2013). Briefly, 6–10 third instar larvae were analyzed for neurometric quantitation from segments A3-A5. For time course analyses, larvae were live imaged at the indicated time point, returned to agar plates, aged at 25°C, and then re-imaged. Images were collected as z-stacks with a step-size of 1.0-2.0 μm and 1024×1024 resolution.

Anti-Form3 polyclonal antibody was generated in rabbits using KLH-conjugated peptides (GenScript, Piscataway, NJ). Form3 epitope (RGSDASSPTRKPSQ (amino acids (aa) 321-334)) was predicted by the GenScript Optimum Antigen design tool. Anti-Form3 antibody was affinity purified against antigenic peptide and specificity confirmed via IHC analyses.

MARCM analysis

MARCM analyses were performed as described (Sulkowski *et al.* 2011). Briefly, *form3^{Em31}*, *FRT^{2A}* or *form3^{Em41}*, *FRT^{2A}* flies were crossed to *GAL4⁵⁻⁴⁰*, *UAS-Venus*, *SOP-FLP⁴²*; +; *tubP-GAL80*, *FRT^{2A}* flies (DGRC stock 109-950). Third instar larvae with GFP-labeled *form3* mutant neurons were subjected to live confocal microscopy.

Neuromorphometric quantification and multichannel reconstructions

Quantitative neurometric analyses were performed as previously described (Das *et al.* 2017). Maximum intensity projections of z-stacks were exported using Zen blue software. Exported images were manually curated to eliminate non-specific auto-fluorescent spots such as larval denticle belts using a custom designed program, *Flyboys* (available upon request). Images were processed, skeletonized, and neurometric data compiled as described (Iyer *et al.* 2013). Quantitative neurometric information was extracted and compiled using custom Python algorithms (available upon request). The custom Python scripts were used to compile the output data from the Analyze Skeleton ImageJ plugin, and the compiled output data were imported into Excel (Microsoft). Neurometric data were analyzed in Microsoft Excel and statistical tests were performed and plotted in GraphPad Prism 9. For Sholl analysis, we used Image J (Ferreira *et al.* 2014) to plot the number of intersections as a function of distance from the cell soma; to determine the peak of maximum branch density (critical value / # of intersections) and corresponding radius. For Strahler analysis, we used the centripetal labeling function

of NeuronStudio (Wearne *et al.* 2005). Dendritic terminals are defined as Strahler order 1. Order increases when 2 or more branches of the same order intersect at a branching point.

Multi-signal cytoskeletal reconstructions and quantitative analyses were performed using a previously describe protocol (Nanda *et al.*, 2020), slightly modified from the protocol used in Das *et al.*, 2017. Briefly, two channel (GFP for F-actin and RFP for MT) image stacks (.czi file format) were first processed in Fiji (Schindelin *et al.* 2012) where a third pseudo-channel was created by adding the signals from the two original channels. Multiple image tiles of a single neuron, if present, were stitched together in Vaa3D (Peng *et al.* 2014). These finalized image files were manually reconstructed using the reconstruction tool neuTube (Feng *et al.* 2015). The newly reconstructed SWC files (Cannon *et al.* 1998, Nanda *et al.*, 2018) were topologically repaired in batch, using custom scripts built within the TREES toolbox (Cuntz *et al.* 2010) environment in MATLAB (MathWorks, Natick, MA). These repaired SWC files are once again opened in neuTube, where additional editing, and quality checks were conducted. The corrected reconstruction files and the image stacks were used as input in the Vaa3D multi-channel plugin (Nanda *et al.*, 2018) to create enhanced reconstructions that represent the morphology along with the intensity and volume occupied by each channel. The neurons were then scaled (from voxel to physical dimension) and their cytoskeletal morphometrics (subcellular and overall structural features) were quantified using custom quantification scripts (download Quantification scripts from dx.doi.org/10.17632/wpzd2wxtgn.1).

Cytoskeletal quantity (MT or F-actin quantity) of a compartment is defined as the product of three parameters: (i) Portion of the volume inhabited by the cytoskeletal signal, (ii) Mean signal intensity and (iii) Compartment volume. All cytoskeletal quantities are represented relative to Class IV WT. MT and F-act quantities are normalized by an M-factor and an F-factor, where the two factors are the inverse of average total MT and average total F-actin of Class IV WT neurons, respectively. Dendrite length, microtubule and F-actin quantities (in the y-axis of Fig. 2J-M, Fig. 3Q-S; Fig. 5J,K) represent the total sum of length, microtubule and F-actin respectively, at each Strahler order and within

every 40- μm path distance bin. These values are computed for each neuron first, and then averaged across all neurons of a given neuron type.

Tubulin photoconversion assay

For analyses of MT stability/turnover, alpha tubulin 84B tagged with photoconvertible tdEOS (*UAS-alphatub84B.tdEOS*), and *UAS-form3-IR* were expressed under the control of *GAL4⁴⁷⁷*. For controls, *GAL4⁴⁷⁷;UAS-alphatub84B.tdEOS* flies were outcrossed to wild-type flies. Photoconversion experiments were carried out following previously described procedures (Tao *et al.* 2016). Briefly, $\sim 30\mu\text{m}^2$ region of the dendrite near the cell body was photoconverted from green to red by exposing to 405nm laser. The photoconverted neurons were live imaged immediately after photoconversion (0h) and at regular intervals of 30 minutes up to 2 hours. Red fluorescent intensities were measured in this photoconverted region and a neighboring non-converted (green fluorescent) region in Zen blue lite (Zeiss). The remaining fluorescence intensity (FI) was measured according to the following formula: $(\text{FI}_{\text{converted}} - \text{FI}_{\text{neighboring}})_{\text{timecourse}} / (\text{FI}_{\text{converted}} - \text{FI}_{\text{neighboring}})_{0\text{h}}$ as previously described (Tao *et al.* 2016).

Biochemical assays

Coding sequences of the Form3 FH1-FH2 and FH2 domains were cloned in *EcoRI* cut pGEX2T vector. The resulting plasmids were used to express FH1-FH2 and FH2 only fragments of Form3 as GST fusion proteins in BL21 *E. coli*. Protein purification was carried out as previously described (Barkó *et al.* 2010) with minor modifications. For MT binding assays, MTs were assembled from tubulin protein (Cytoskeleton, Inc.) according to the vendor's instructions. In MT co-sedimentation assays, GST::Form3-FH1-FH2 and GST::Form3-FH2 proteins were pre-cleared by ultracentrifugation, then they were diluted in MT binding-buffer (MBB; 10 mM Na-HEPES pH: 7.0, 1 mM MgCl_2 , 1 mM EGTA, 1 mM DTT, 20 μM taxol, 0.5 mM thesit, 10% glycerol) and mixed with pre-assembled MTs (0.5 μM). Control samples did not contain MTs. Protein mixtures were incubated for 30 min at room

temperature then centrifuged at 100,000 X g for 1 h at 25°C. Proteins in the supernatants and pellets were resolved by SDS-PAGE then stained with colloidal Coomassie-blue. In GST pull-down assays, purified Form3 proteins were immobilized on glutathione-S-sepharose beads, followed by incubation with taxol-stabilized MTs (0.5 μM) for 30 min at room temperature in MBB. The beads were washed thoroughly in MBB followed by protein elution in SDS-PAGE sample buffer and detection by anti-GST (Sigma) and anti- α -tubulin (Sigma) Western blot.

Generation of form3 RNAi-resistant and human INF2 transgenes

A synthetic RNAi-resistant *UAS-form3* transgene (*UAS-form3-IR^R*) was generated as previously described (Schulz et al., 2009; Jonchere and Bennett, 2013). Briefly, codon usage of the *form3-RA* transcript was modified by the introduction of silent mutations to the RNAi target sequence for the *form3-IR* transgene predominantly used in this study (B32398; TRiP reagent ID: HMS00393) in order to render the transgene resistant to RNAi-mediated knockdown. The RNAi target sequence is located in the N-terminal Form3 FH3 domain and the synthetic RNAi-resistant sequence covered amino acids 63-80 of the Form3-PA protein isoform which is identical to the sequence in the other Form3 protein isoform, Form3-PB. The silent mutations were selected to minimize the use of rare codons recognized by low abundance tRNA species over a 54 bp segment of the coding sequence corresponding to amino acids 63-80 while the remainder of the *form3* coding sequence was unaltered (Supplemental Materials and Methods). Gene synthesis was performed by GenScript (Piscataway, NJ) and synthetic DNA was subcloned in using EcoRI (5') and Kpn I (3') into *pUAST-attB*. Transgenic *UAS-form3-IR-R* strains were generated by Φ C31-mediated integration with targeting to 2R (*VK1*) (GenetiVision, Houston, TX).

For optimal expression, we synthesized *D. melanogaster*-codon-optimized INF2 cDNAs (GenScript, Piscataway, NJ). Two custom gene syntheses were performed to generate a full-length cDNA and a cDNA in which the DID and DAD autoinhibitory regulatory domains had been deleted, leaving only the FH1 and FH2 domains (FH1-FH2). Each synthesized gene was C-terminally FLAG-

tagged (DYKDDDDK) and subcloned into *pUAST-attB*. Transgenic INF2 strains were generated by Φ C31-mediated integration with targeting to 2L (*attP40*) (GenetiVision, Houston, TX).

Behavioral assays

For noxious heat nociceptive assays, age-matched third instar larvae were recovered and briefly rinsed with water to remove any residual media. Larvae were then transferred to a black aluminum metal plate which was pre-sprayed with water to generate a thin film facilitating larval movement. Larvae were allowed to acclimate to the plate and resume normal peristaltic locomotion before the plate was transferred to a temperature-controlled Peltier plate (TE Technology). The temperature was preset to 45°C to evoke nocifensive behaviors. Heat-evoked behaviors were recorded using a Nikon D5300 DSLR camera. Video files were processed using ImageJ and manually curated to evaluate response latency and characterize nocifensive behaviotypes (Chattopadhyay *et al.* 2012). The maximal latency period for behavioral response was set at 20 s after stimulus, and larvae that failed to exhibit a behavioral response in this interval were classified as non-responders.

Statistics and data availability

Data are reported as mean, and error bars represent standard error of the mean (SEM) or standard error of proportion (SEP) as indicated in figure legends. Data represent biological replicates with the exception of the Western blots for the GST pull-down assays, which represent technical replicates. Sample sizes were selected based upon accepted norms in the published literature and included both sexes in all analyses. Statistical analyses (reported in the figure legends) were performed using either one-way ANOVA with Bonferroni correction for multiple comparisons; Kruskal-Wallis test with Dunn correction for multiple comparisons; two-way ANOVA with Bonferroni correction; Mann-Whitney U test; or unpaired t-test. All datasets were tested for normality (Shapiro-Wilk normality test)

and homogeneity of variance (Bartlett's test or F test) before statistical analysis. All new genotypes presented here are available upon request. Digital reconstructions of neuronal morphology have been deposited into the NeuroMorpho.Org database (Ascoli 2006) for public distribution under the Cox and Ascoli archives.

Results

form3 regulates dendritic arborization in Drosophila nociceptive neurons

Molecular control of cytoskeletal organization and dynamics is essential in specifying, stabilizing, and modulating dendritic architecture. We previously conducted a systematic neurogenomic-driven genetic screen to identify putative cytoskeletal regulators of dendritic arborization using *Drosophila* Class IV (CIV) nociceptive sensory neurons as a model system (Das *et al.* 2017). We identified CIV expression of multiple members of the Formin gene family, including *form3* and *Frl* (Das *et al.* 2017). Formins have been demonstrated to function by regulating the F-actin and MT cytoskeletons; however, their role(s) in neuronal development, and more specifically dendritogenesis, remain incompletely understood (Galbraith and Kengaku, 2019). Therefore, we performed a pilot RNAi screen to examine potential functional roles of the six *Drosophila* Formins. Our screen revealed *form3* knockdown (*form3-IR*) produced severe defects in CIV dendritic arborization (Figure 1B; Figure S1A-H). Based upon these results, we chose to conduct more in-depth phenotypic studies of *form3* function in dendritic morphogenesis.

CIV-specific *form3-IR* expression led to severe dendritic reductions, resulting in a highly rudimentary arbor with pronounced defects in distal higher order branching (Figure 1A,B,E,F,G,I). Dendritic branch order analyses showed significant reductions in higher branch orders (Strahler order 2) compared to control, with Strahler order 1 branches, representing terminals that account for the majority of control CIV branches, being undetectable in *form3-IR* neurons (Figure 1G). To quantify effects on

dendritic branch distribution, Sholl analyses were used to plot the density profiles of branches as a function of distance from the soma and to compare the peak of maximum branch density (critical value) and its corresponding radius. Both parameters showed significant reductions in CIV-specific *form3-IR* expression (Figure 1I).

To independently validate phenotypic defects observed with *form3-IR*, we conducted MARCM clonal analyses using two previously published *form3* point mutant alleles, namely *form3^{Em31}* and *form3^{Em41}* (Tanaka *et al.* 2004). Consistent with *form3-IR* analyses, MARCM mutant clones exhibited defects in CIV dendritic arborization characterized by short interstitial branches and reductions in distal terminal branching (Figure 1C,D). Morphometric analyses revealed significant reductions in terminal dendrites and concomitant reductions in total dendritic length (Figure 1E,F). Moreover, Strahler analyses showed a similar result to that observed with *form3-IR*, where the reduction was observed in 2nd order branches with a complete loss of the terminal 1st order branches for both *form3* mutant alleles (Figure 1H). Sholl analyses identified a significant reduction in the critical value for both *form3^{Em31}* and *form3^{Em41}* (Figure 1J).

Collectively, our phenotypic analyses revealed relatively stronger phenotypic defects in *form3-IR* knockdowns compared to the *form3^{Em31}* or *form3^{Em41}* MARCM clones, which were comparatively similar in their phenotypic defects. This variability could be due to different effects of these genetic perturbations on Form3 protein levels. To address this question, we developed polyclonal antibodies against Form3 and investigated expression in control vs. mutant backgrounds. Form3 is expressed in da neuron subclasses including CIV neurons in control third instar larvae (Figure S11-I''). To assess antibody specificity and explore how *form3-IR* or *form3* mutant alleles impact Form3 expression levels, we performed immunohistochemistry (IHC) analyses to compare Form3 protein levels in control, *form3-IR* and *form3^{Em41}* MARCM clone CIV neurons. Form3 levels were reduced by 77% in *form3-IR* CIV neurons and by 44% in *form3^{Em41}* mutant CIV neurons relative to control levels (Figure 1K-O). These data indicate that *form3* knockdown in CIV neurons results in a stronger reduction of Form3 levels

relative to the *form3*^{Em41} mutant neurons which is consistent with the phenotypic variability observed in these genetic backgrounds.

To determine if we could alleviate the loss-of-function dendritic defects observed with *form3* knockdown, we generated a *UAS-form3-IR* resistant transgene (*UAS-form3-IR^R*) in which we introduced silent mutations in the *form3-IR* target sequence to render the transgene resistant to RNAi-mediated knockdown while limiting the use of rare codons that are recognized by low abundance tRNAs. We expressed this transgene in the *form3-IR* background of a CIV neuron and observed a partial, albeit significant, rescue with respect to number of dendritic branches and total dendritic length (Figure S2A-E). While the RNAi-resistant transgene did not fully rescue the *form3-IR* mediated dendritic defects this could potentially be due to the relative strength of the *form3-IR* and/or insufficient levels of expression required to fully restore the dendritic abnormalities though the introduction of the silent mutations using less common codon usage. Alternatively, it is possible that the failure to fully rescue the *form3-IR* defects could be due to expression timing and levels that do not precisely mirror endogenous Form3 expression.

Collectively, these data indicate that Form3 promotes the appropriate number and position of branches along the proximal-distal axis of dendritic arbors, and is required to promote higher order branches. Given that *form3-IR* produced the strongest phenotypic defects in CIV dendritogenesis coupled to the strongest reduction in Form3 protein levels, and that the *form3* homozygous mutant alleles are lethal prior to the third instar larval stage, we performed the remainder of our loss-of-function (LOF) studies using *form3-IR*.

form3 regulates dendritic microtubules

Formins are well known regulators of the cytoskeleton and thus we hypothesized that *form3* functions to modulate dendritic architecture. We utilized CIV-*GAL4*-driven expression of transgenic multi-fluor cytoskeletal reporters in combination with *form3-IR* in order to simultaneously visualize the

F-actin (*UAS-GMA*) and MT (*UAS-mCherry::Jupiter*) cytoskeletons *in vivo* (Das *et al.* 2017). These studies revealed disruptions in F-actin cytoskeletal distribution and a severe reduction of dendritic stable MTs (Figure 2A-B”). To verify the observed defects on dendritic stable MTs was not due to a non-specific effect of *form3-IR* on expression of the mCherry-tagged microtubule-associated protein (MAP) Jupiter, we performed independent validation experiments. IHC analyses of CIV neurons expressing *form3-IR* or *form3^{Em41}* CIV MARCM clones were performed using antibodies against the *Drosophila* MAP1B molecule Futsch. Futsch is a known MAP that both stabilizes MTs and has been shown to be a marker of the stable MT population (Halpain and Dehmelt 2006; Hummel *et al.* 2000; Roos *et al.* 2000). Compared to genetic control CIV neurons, Futsch levels were reduced by 55% in *form3-IR* neurons at the cell body (Figure 2C-D”,G). We also observed a 48% reduction in Futsch labeling at the cell body in *form3^{Em41}* MARCM clones when compared to control MARCM clones (Figure 2E-F”,G). These analyses collectively suggest that *form3* has a major functional role in regulating a population of stable dendritic MTs.

To assess the effect of *form3* disruption on the cytoskeleton across the dendritic arbor, we employed newly developed next generation multichannel neuronal reconstructions (Das *et al.* 2017; Nanda *et al.*, 2020). Multichannel reconstructions of cytoskeletal features revealed *form3*-mediated alterations in F-actin distribution and stable MT levels with *form3-IR* knockdown (Figure 2H-I”). Alterations in F-actin organization upon *form3* knockdown manifest as reduction in the critical value (the peak of the curve) and a proximal shift of the critical radius (the radius at which the peak of the curve lies) of the relative F-actin quantity (Figure 2J). We found a complete absence at Strahler order 1 in *form3* knockdown, which makes up the majority of the F-actin rich terminal branches in control CIV neurons (Figure 2K). As predicted, the effect on MTs was severe, as revealed by overall reductions in the relative MT quantity, as well as reductions at branch orders 2-5 and a complete absence of Strahler order 1 terminals (Figure 2L,M).

form3 is required for dendritic growth in late larval development

To assess how *form3* may contribute to dendritic arborization over developmental time, we conducted time course studies examining CIV-specific *form3* knockdown at first, second, and third instar larval stages. These analyses revealed that *form3-IR* mediated defects in dendritic hypotrophy increase as a function of developmental age (Figure 3A-H). Phenotypic comparisons at the second instar stage revealed a modest qualitative increase in short interstitial branches emanating from the lower order dendrites in *form3-IR* (Figure 3 B,B',F,F'), whereas third instar *form3-IR* neurons exhibited dramatic reductions in dendritic branches (Figure 3C,C',G,G'). However, quantitative analyses revealed no significant difference in the number of branches or total dendritic length at first or second instar stages when compared to control, but a severe reduction in both length and branch number at the third instar stage (Figure 3I,J). To address putative effects of maternal perdurance, we also investigated disruption of *form3* function in the embryonic germline and CIV neurons using *nanos-GAL4* to drive expression of *form3-IR* (Ye *et al.* 2004). As with CIV-specific *form3* disruption (Figure 3), morphometric analyses again revealed no significant difference in number of branches or total dendritic length at the first or second instar stages; however, third instar larvae displayed reductions in both morphometric parameters (Figure S3A,B). As control CIV dendrites continue to grow and space-fill the receptive field over development (Figure 3D), whereas *form3*-depleted CIV neurons exhibit a progressive loss of dendrites over development (Figure 3H), these data suggest that the *form3-IR* phenotype exhibits a slowed growth, particularly at later stages of larval development.

A recent study demonstrated that dendritic arbor length of multiple da neuron subclasses at the third larval instar stage, including CIV neurons, is highly interrelated with local MT quantities (Nanda *et al.* 2020). Given the effect of *form3-IR* on dendritic growth and stable MTs at the third instar stage and the progressive loss of terminal branches observed in time course analyses, we hypothesized that slowed dendritic growth and loss of dendritic branches correlates with progressive reduction in the population of stable MTs over development. Consistent with this hypothesis, we found that stable MT signal is

likewise progressively reduced over the developmental time in *form3*-depleted CIV neurons relative to controls (Figure 3K-P). Quantitative analyses revealed significantly reduced relative MT quantities on the dendritic arbor over developmental time in *form3-IR* neurons (Figure 3Q-S). Despite these reductions at first or second instar larval stages, we did not identify a significant change in either total dendritic length or terminal dendrites for *form3-IR* neurons, whereas third instar larval mutant neurons were reduced for both metrics. These findings may suggest that while stable MT levels are reduced in early larval stages, the remaining population of stable MTs is sufficient to support arborization, whereas in the third instar stage the level of stable MTs dips below a critical threshold required to sustain the growth of the complex, space-filling dendritic arborization profile of CIV neurons.

form3 regulates higher order branching

As *form3* disruption produces severe defects in higher order dendritic branching, we sought to test a hypothesis that *form3* overexpression may lead to excessive terminal branching. We overexpressed *UAS-form3* in CIVs, which revealed a shift in branching distribution characterized by a reduction in branching immediately proximal to the cell body as well as exuberant terminal branching and elongated terminal dendrite extension (Figure 4A-B'). Sholl analysis revealed a significant increase in the critical value (Figure 4C), which occurs prominently around 105-200 microns from the soma (Figure 4D). Moreover, Strahler analysis revealed a significant increase in the number of terminal branches, indicated by Strahler order 1 (Figure 4E).

Another striking feature observed with *form3* overexpression is a change in primary dendrite branch thickness. Relative to control, primary branch diameter was notably increased by *form3* overexpression (Figure 4A',B', arrowheads), suggesting increased Form3 levels may alter underlying cytoskeletal organization. Therefore, we sought to assess the effect of *form3* overexpression on the cytoskeleton. Multichannel cytoskeletal reconstructions revealed an altered F-actin signature in CIV neurons overexpressing Form3, which when quantified revealed a leftward shift of the critical value

(peak of the curve) indicating an increase in relative F-actin quantity in the first few dendritic branch orders (Figure 4H'',I'',J). Furthermore, cytoskeletal analyses revealed Form3 overexpression leads to an increase in the MT intensity profile proximal to the cell body (Figure 4H',I',K) suggestive of a role for Form3 in promoting MT density in primary dendritic branches. This raises the question of whether there may be changes in the cytoskeletal organization of dendritic terminals as well. Relative to control terminals (Figure 4F,F'), Form3 overexpression qualitatively increased MT signal into the elongated terminal branches, potentially promoting their extension (Figure 4G,G').

In light of the partial rescue we observed with expression of the *UAS-form3-IR^R* transgene in the *form3-IR* mutant background, we examined the effects of overexpressing the RNAi-resistant transgene to determine whether it may phenocopy aspects of the *form3* overexpression phenotype. These analyses revealed a qualitatively similar phenotype with thickened primary dendrites and clustered, elongated higher order branches (Figure S4A-C). Sholl analyses revealed no statistical difference in the critical value or radius between *UAS-form3* and *UAS-form3-IR^R* suggesting that the RNAi-resistant version can recapitulate phenotypic features of the unmodified *UAS-form3* transgene (Figure S4D).

form3 directly interacts with microtubules

Based on the regulatory relationship between Form3 function and MT architecture, we sought to examine potential direct or indirect interactions between Form3 and MTs. To address this, we performed MT co-sedimentation (\pm MTs) and MT precipitation assays using GST-tagged Form3 constructs expressing either the FH1-FH2 domains or the FH2 domain alone as compared to GST controls lacking Form3 sequences. Analyses of FH1-FH2 fusion proteins revealed specific co-sedimentation in pellet fractions only in the presence of MTs (Figure 5A) indicative of a direct interaction. Analyses of the FH2 domain alone revealed low level self-pelleting in the absence of MTs. Despite this, there was a notable increase in the amount of FH2 fusion protein that co-sedimented with MTs specifically, suggesting the FH2 domain is sufficient for Form3-MT direct interaction. To further validate these results, we

performed MT precipitation assays, revealing tubulin precipitated only in the presence of the Form3 constructs, but not with GST alone (Figure 5B).

Since the effects of *form3* disruption were severe on MTs, we investigated the potential role of Form3 in regulating MT dynamics. To this end, we used a previously described approach, where we expressed α -tubulin tagged with photoconvertible tdEOS in CIV neurons (Herzmann et al., 2017; Tao et al., 2016). When exposed to 405nm light, tdEOS converts from green to red and the duration for which the red signal lasts can be used to assess MT turnover. We photoconverted a small segment of the dendrite close to the cell body in controls and *form3-IR* third instar larvae and imaged the animals at 30-minute intervals for 1 hour (Figure 5C-D'''). Our results showed that there was no significant difference in the red fluorescent intensities (pseudo-colored magenta) between control and *form3-IR* animals over the course of our analyses suggesting that the rate of MT turnover is similar in both these groups (Figure 5E). However, it is important to note that *form3-IR* animals have significantly less MT signal to begin with when compared to control (Figure 5F). To assess whether a 1 hour time interval may be too short to observe MT dynamics, we extended our time-lapse analyses to 2 hours and our results remained the same that there was no statistical difference in the rate of turnover for the subpopulation of MTs that remain in *form3*-depleted neurons (Figure S5). This raises the possibilities that Form3 may play a role in MT dynamics via *de novo* MT generation, or alternatively that Form3 may only function in stabilizing a subset of MTs that are normally bound by MAPs including Futsch and Jupiter. We attempted to visualize *de novo* MT generation and dynamics using a EB1::GFP +TIP labeling (Rolls et al., 2007; Ori-McKenney et al., 2012; Arthur et al., 2015) in *form3-IR* CIV neurons, however, the EB1::GFP signal in *form3*-depleted was below the level of detection for reliable quantification (data not shown). Thus, we can neither rule in, nor rule out, the possibility of a role for Form3 in *de novo* MT generation/dynamics. The most parsimonious explanation of our data is the Form3 has a role in regulating at least a subpopulation of stable MTs while a remaining MT subpopulation in *form3* deficient neurons are not more unstable than controls.

form3 is required for dendritic localization of mitochondria and satellite Golgi

Collective evidence implicates Form3 in MT stability, which while clearly critical to supporting dendritic complexity may not fully explain why the arbor exhibits pronounced hypotrophy at the late larval stage. Therefore, we sought to examine the potential functional consequences of a destabilized MT cytoskeleton by examining localization of organelles essential for supporting dendritic development. Studies have demonstrated that defects in mitochondrial localization can lead to dendritic degeneration/fragmentation in both invertebrates and vertebrates (Tsubouchi *et al.* 2009; Lopez-Domenech *et al.* 2016). Moreover, INF2 (human ortholog of Form3) has been shown to affect mitochondrial length and ER-mitochondrial interactions (Korobova *et al.* 2013). *In vivo* imaging revealed defects in dendritic mitochondria localization in *form3-IR* neurons, whereas proximal axonal localization appeared largely normal (Figure 6A-B’). We also observed a significant decrease in dendritic mitochondria density (Figure 6C). These data suggest that mitochondria localization is at least in part dependent on Form3, as well as a stable MT cytoskeleton.

Localization of satellite Golgi has been demonstrated to play key roles in regulating dendritic development and MT nucleation (Ye *et al.* 2007; Ori-McKenney *et al.* 2012). We hypothesized that *form3* disruption impairs proper localization of satellite Golgi due to a disrupted MT cytoskeleton, which could, in part, contribute to the observed dendritic hypotrophy. We discovered aberrant localization in *form3-IR* neurons, with the majority of the satellite Golgi confined to the proximal branches, though we did observe some Golgi in the terminals (Figure 6D-E’). The density of satellite Golgi was also significantly reduced (Figure 6F). In controls, there was a distinct localization of satellite Golgi to dendritic branch points, which was often not the case in *form3-IR*. In addition, while controls display “islands” of fused Golgi located along interstitial branches, such islands are not observed with *form3-IR*, but rather only small puncta (Figure 6D,E). These data suggest that an intact MT cytoskeleton contributes to normal satellite Golgi translocation, and that defects in localization may contribute to overall dendritic hypotrophy observed in *form3-IR* neurons.

INF2 can partially alleviate form3 depletion defects in dendrite complexity and stable MTs

To investigate the hypothesis that *Drosophila* Form3 and human INF2 share conserved functions, we generated transgenic fly strains to allow for inducible expression of either full length INF2 or a truncated version in which autoinhibitory regulatory domains (DID/DAD) were deleted, leaving only the FH1 and FH2 domains (FH1-FH2) (Figure 7A). Previous studies in *C. elegans* revealed that removal of the DID/DAD inhibitory domains was required for INF2 rescue of the worm ortholog *exc-6* (Shaye and Greenwald 2015), and Form3 protein does not contain the DID/DAD domains.

We initiated our *INF2* analyses by first examining the functional consequences of overexpressing these transgenes in CIV neurons. Overexpression of the full length *INF2* transgene (Figure S6A) modestly reduced the number of terminal branches, but had no significant impact on total dendritic length (Figure S6B,C), whereas overexpression of the truncated *INF2-FH1-FH2* transgene (Figure 7E) did not significantly alter the number of terminal branches or total dendritic length relative to control CIV neurons (Figure 7F,G). To determine whether INF2 expression can alleviate morphological defects observed in *form3*-depleted neurons, we introduced the *INF2-FH1-FH2* variant into the *form3-IR* genetic background and out-crossed to a *CIV-GAL4* driver. These analyses revealed a modest, but significant, recovery of CIV morphological defects (Figure 7C,D) by mildly increasing the number of terminal dendrites and total dendritic length (Figure 7F,G). Sholl analyses further revealed a significant increase in the critical radius with *INF2-FH1-FH2* expression indicative of an increase in dendritic complexity (Figure 7H).

As *form3* disruption severely reduces the expression of markers for stable MTs (Figure 2), we hypothesized that introduction of *INF2-FH1-FH2* may be able to partially recover Futsch labeling on dendrites of *form3*-depleted neurons. Consistent with this hypothesis, analyses revealed an increase in Futsch labeling on the soma and dendrites of CIV neurons with *INF2-FH1-FH2* expression (Figure 7I-I') relative to what we observed with *form3-IR* knockdowns (Figure 2D-D'). These studies indicate that *INF2-FH1-FH2* can partially alleviate *form3-IR* mediated defects in dendritic complexity and stable

MTs. Collectively, these analyses suggest a degree of functional conservation between Form3 and INF2, via FH1-FH2, in promoting dendritic complexity and MT stability.

Roles of form3 and INF2 in peripheral sensitivity and thermosensory nociception

CIV neurons function as polymodal nociceptors and are required to mediate a variety of nocifensive responses including an aversive body rolling (360°) in larvae upon exposure to potentially damaging thermal, chemical, or mechanical stimuli (Tracey *et al.* 2003; Hwang *et al.* 2007; Lopez-Bellido *et al.* 2019; Himmel *et al.* 2019; Himmel *et al.* 2017). Furthermore, recent evidence connects defects in dendritic architecture with noxious heat-evoked nocifensive behavioral sensitivity (Honjo *et al.* 2016). We hypothesized that *form3* disruption in these neurons may lead to reduced peripheral sensitivity to noxious heat and thereby impair nocifensive behavior. Thus, we expressed *form3-IR* in CIV neurons and observed nocifensive behavioral responses when challenged with a noxious heat (45°C) stimulus. These analyses revealed a severe impairment in noxious heat evoked behavioral responses (Figure 8B,E,F; Movie S1), indicating a dramatic loss of peripheral sensitivity. This behavioral defect was not due to any general defect in locomotion, as both control and *form3-IR* larvae exhibit normal locomotor behavior. CIV-specific inhibition of *form3* led to a dramatic increase in the latency to respond (among those few larvae which responded) (Figure 8A,B,E). The majority of *form3-IR* larvae were classified as non-responders, as they failed to exhibit rolling or other documented nocifensive behaviors within the 20 second assay period (Figure 8B,F).

We further sought to determine whether *form3* or *INF2-FH1-FH2* overexpression leads to changes in heat-induced nocifensive behavior. We found that neither *form3* nor *INF2-FH1-FH2* overexpression resulted in a significant change from controls with respect to latency (Figure 8C-E); however, we did observe a reduction in the percentage of responders in both these conditions (Figure 8F). Apart from nocifensive rolling, several other noxious heat-evoked behaviootypes have been described, including larval whipping, head thrashing, and seizures (Chattopadhyay *et al.* 2012). Relative to controls, and

among those larvae that failed to execute rolling behavior, these behaviors were variably observed with greater incidence in *form3* and *INF2-FH1-FH2* overexpression, as well as to some modest extent in *form-IR* (Figure 8F). This may suggest that the alterations in dendritic morphology observed with *form3* or *INF2-FH1-FH2* manipulations impair normal processing of thermal stimuli, resulting in altered behavioral repertoires.

Intriguingly, mutations in *INF2* have been causally linked to CMT disease, yet the mechanisms of action in CMT pathology are incompletely understood (Boyer *et al.* 2011). Neurological features of CMT include peripheral motor and sensory neuropathies, and the primary phenotypes consist of progressive distal muscle weakness and atrophy, reduced tendon reflexes, foot and hand deformities, and peripheral insensitivity (Ekins *et al.* 2015). CMT sensory neuropathies lead to distal sensory loss resulting in a reduced ability to sense heat, cold, and pain, yet the neural bases of these sensory defects remains to be fully elucidated. Given the causative role of *INF2* mutations in CMT disease and the impaired distal sensitivity to thermal stimuli in CMT patients, we next tested the hypothesis that introduction of the *INF2-FH1-FH2* transgene into the *form3-IR* background may rescue the impaired behavioral responses to noxious thermal stimuli. We found that CIV expression of *INF2-FH1-FH2* significantly rescued the behavioral latency defects observed in *form3-IR* larvae leading to an increase in the percentage of behavioral responders (Figure 8D-F; Movie S2). While the introduction of *INF2-FH1-FH2* only partially rescues the behavioral defects, it nonetheless suggests a conserved role for *Form3* and *INF2* in regulating peripheral sensitivity to noxious stimuli that has potential implications for the etiological bases of CMT peripheral sensory neuropathy.

Previous studies have linked CMT2C to aberrant Ankyrin repeat (ARs) in the human TRPV4 channel (Landouré *et al.* 2010). Noxious heat detection in *Drosophila* larvae requires the function of two TRPA channels, *Painless* and *TRPA1*, both of which contain ARs (Tracey *et al.* 2003; Zhong *et al.* 2012). In the mechanosensing TRP channel *NompC*, ARs provide direct linkage of the channel to the MT cytoskeleton and are required for mechanical gating of the channel (Zhang *et al.* 2015). Moreover,

studies of Painless have revealed that its AR domains are necessary for thermal, but not mechanical, nociception (Hwang *et al.* 2012). These findings led us to hypothesize that *form3*-mediated defects in the MT cytoskeleton may affect localization of AR-containing TRP channels such as Painless. To investigate this hypothesis, we conducted *in vivo* imaging of CIV neurons expressing *UAS-Painless^{p103}::VFP* while simultaneously expressing *form3-IR*. In contrast to controls, in which *Painless^{p103}::VFP* is strongly expressed on CIV cell bodies, as well as throughout dendrites and proximal axons (Figure 8G-G''), in *form3-IR* neurons there is a notable reduction of Painless signal on proximal and distal CIV dendrites, despite comparable levels of cell body expression and to a lesser extent axonal expression (Figure 8H-H''). These data suggest that *form3-IR*-induced defects in nocifensive behavior may result from a combination including severely reduced arbor complexity and aberrant localization of channels required for thermosensory nociceptive behavior.

Discussion

form3 function in dendritic arborization and MT stability

Dendritic development is a complex phenomenon, which requires spatio-temporal regulation of local cytoskeletal interactors to direct specific morphological features of the neuron. Molecules involved in this process can have one of many roles, such as arbor specification, growth by enhancement, suppression by reduction, or simply maintenance of the dendritic arbor. Our results suggest Form3 is required in maintaining dendritic arbor growth, as *form3* mutants exhibit progressive dendritic hypotrophy ultimately leading to a highly rudimentary arbor.

The hypothesis that Formins may regulate MTs has been proposed for some time, but only recently have biochemical studies begun to explore how Formins interact with MTs and affect their dynamic properties. Studies have shown that multiple mammalian Formins, as well as the fly Formin Capuccino, can interact directly with MTs (Breitsprecher and Goode 2013; Roth-Johnson *et al.* 2014); however, whether this is a specific or more general property of Formin molecules remains unclear. In

cultured hippocampal neurons, the formin mDia1 has been implicated in MT stabilization with knockdowns leading to increased MT catastrophe and reductions in tyrosinated MTs as well as increased spine density and dendritic complexity (Qu *et al.* 2017). Conversely, Hong *et al.* (2018), demonstrated that knockdown of *mDia1* resulted in reductions in total dendritic length and number of branch points in cultured hippocampal neurons, thus additional studies are needed to clarify the roles of mDia1 in dendritic development. At a mechanistic level, we present multiple converging lines of evidence implicating Form3 in positively regulating a population of stable MTs. Consistent with this, previous studies demonstrate that formation of stabilized MTs requires the Form3 ortholog INF2 (Andrés-Delgado 2012).

form3 function in dendritic organelle localization

Proper mitochondrial function is required to support neuronal development and function, as mitochondria are fundamentally important for several cellular events, such as ATP production and Ca²⁺ regulation, as well as release and reuptake of neurotransmitters at synapses (Detmer and Chan 2007). Several consequences of impaired mitochondrial dynamics have been studied, and it has been shown that mitochondria dysfunction is highly correlated with neurodegenerative diseases (Chan 2006). Mutations in mitochondrial GTPase *mitofusin2* cause autosomal dominant CMT type 2A disease (Zuchner *et al.* 2004), and disruptions in OPA1, a protein that mediates mitochondrial fusion, lead to autosomal dominant optic atrophy, an inherited form of optic nerve degeneration (Alexander *et al.* 2000). Moreover, studies have demonstrated that defects in mitochondrial function, morphology, or trafficking contribute to dendritic degeneration and loss of complexity in both invertebrates and vertebrates. Mutations in the mitochondrial protein Preli-like (Prel), as well as its overexpression, cause mislocalization and fragmentation of mitochondria, leading to dendritic loss via a mechanism involving increased eIF2 α phosphorylation and translational repression (Tsubouchi *et al.* 2009; Tsuyama *et al.* 2017). Disrupted mitochondrial distribution leads to a loss of dendritic complexity in mouse

hippocampal neurons, which precedes neurodegeneration, supporting a critical role of mitochondria in stabilizing complex dendritic architectures and maintaining neuronal viability (Lopez-Domenech *et al.* 2016). These findings are also intriguing in terms of conserved functions between Form3 and INF2, the latter of which has been demonstrated to affect mitochondrial length and ER-mitochondrial interactions (Korobova *et al.* 2013).

In addition to mitochondrial localization defects, we also postulated that defects in MT cytoarchitecture may impair localization of satellite Golgi on the dendritic arbor. Satellite Golgi have been shown to play important functional roles in regulating dendritic growth and branching by serving as local sites for MT nucleation to support branch extension (Ye *et al.* 2007; Ori-McKenney *et al.* 2012). Furthermore, a recent study discovered a role for the formin mDial1 in proper positioning of Golgi to the base of major dendrites in cultured hippocampal neurons (Hong *et al.* 2018). We discovered that *form3*-depleted neurons also exhibited defects in satellite Golgi localization and in gross Golgi architecture. Interestingly, previous studies have implicated INF2 in maintenance of Golgi architecture in cultured cells where disruptions in INF2 function cause Golgi fragmentation (Ramabhadran *et al.* 2011). Combined, these analyses provide important insights into the putative mechanistic bases of *form3*-mediated defects in dendritogenesis, and identify an important role of a stable MT cytoskeleton in supporting the proper localization of dendritic organelles.

Functional conservation of form3 and INF2

Numerous neurological disorders including Lissencephaly, amyotrophic lateral sclerosis, spastic paraplegia, tauopathies, Alzheimer disease and CMT are linked to defects in the MT cytoskeleton and/or MT motor-based transport (Franker and Hoogenraad 2013). We show *form3* is required for dendritic development, while the potential role of *INF2* is unknown with respect to neural development. Morphological defects caused by *form3* disruption can be partially recovered by expression of the INF2 FH1-FH2 domains, with respect to dendritic growth and Futsch labeling of MTs. These analyses suggest

potential evolutionarily conserved functions between *form3* and *INF2* in regulation of dendritic architecture and MTs.

Mutations in *INF2* are known to be causative for CMT disease (Boyer *et al.* 2011), although the mechanistic functions of *INF2* in disease pathogenesis are unclear. We observed that *form3* disruption in CIV nociceptive neurons severely impairs noxious heat evoked behavioral responses resulting in peripheral insensitivity, which is consistent with sensory neuropathies observed in CMT patients. Intriguingly, we can partially revert this heat insensitivity by the introduction of *INF2* FH1-FH2 in the *form3* mutant background, revealing not only partial morphological recovery, but also behavioral rescue.

Previously, CMT diseases have been characterized by progressive defects in axonal development, myelination, protein translation, and intracellular traffic of vesicles and organelles (Bucci *et al.* 2012; Niehues *et al.* 2014). CMT disease has also been linked to various defects in mitochondrial dynamics with CMT causing mutations altering energy production via a mitochondrial complex I deficiency (Cassereau *et al.* 2011). Our work, in addition to these mechanisms, suggests a possible additional mechanism whereby aberrant *INF2* activity may lead to progressive sensory neuron dendritic hypotrophy that could dramatically reduce dendritic field coverage and contribute to peripheral insensitivity. CMT sensory neuropathies manifest as impaired peripheral sensitivity to heat, cold and pain and mutations in thermosensitive TRP channels such as TRPV4 have been linked to CMT2C (Landouré *et al.* 2010). We discovered that *form3* mutant CIV nociceptive sensory neurons exhibit defects in dendritic localization of the thermosensitive TRPA channel Painless. Interestingly, previous work demonstrates that the heat sensitive TRPV1 channel is known to bind to MTs and disruption of the MT cytoskeleton leads to attenuation of TRPV1 currents impacting desensitization (Goswami *et al.* 2011; Lainez *et al.* 2010; Ferrandiz-Huertas *et al.* 2014). TRPV1 physically interacts with MTs and an intact MT cytoskeleton is required to preserve TRPV1 function as MT disassembly by treatment with colchicine impairs TRPV1 membrane insertion revealing a role in ion channel trafficking to the membrane (Goswami *et al.* 2007; Goswami 2012; Storti *et al.* 2012). Given that *form3* mutant neurons

exhibit dendritic MT defects and aberrant TRP channel localization, disruptions in these biological processes may contribute to the behavioral insensitivity to noxious heat observed in *form3* mutants. Combined, our findings provide new insights into the roles of formins in dendritic development and may provide novel mechanistic insights into the potential etiological bases of INF2-mediated CMT sensory neuropathy.

References

- Alexander C, Votruba M, Pesch UE, Thiselton DL, Mayer S, Moore A, Rodriguez M, Kellner U, Leo-Kottler B, Auburger G, Bhattacharya SS, Wissinger B (2000) OPA1, encoding a dynamin-related GTPase, is mutated in autosomal dominant optic atrophy linked to chromosome 3q28. *Nat Genet* 26:211-215.
- Andrés-Delgado L, Antón OM, Bartolini F, Ruiz-Sáenz A, Correas I, Gundersen GG, Alonso MA (2012) INF2 promotes the formation of deetyrosinated microtubules necessary for centrosome reorientation in T cells. *J Cell Biol* 198:1025-1037.
- Arthur AL, Yang SZ, Abellana AM, Wildonger J (2015) Dendrite arborization requires the dynein cofactor NudE. *J Cell Sci* 128(11):2191-2201.
- Ascoli GA (2006) Mobilizing the base of neuroscience data: the case of neuronal morphologies. *Nat Rev Neurosci* 7:318-724.
- Barkó S, Bugyi B, Carlier MF, Gombos R, Matusek T, Mihály J, Nyitrai M (2010) Characterization of the biochemical properties and biological function of the formin homology domains of *Drosophila* DAAM. *J Biol Chem* 17:13154-13169.
- Bartolini F, Gundersen GG (2010) Formins and Microtubules. *Biochim et Biophys Acta* 1803:164–173.
- Boyer O, Nevo F, Plaisier E, Funalot B, Gribouval O, Benoit G, Huynh Cong E, Arrondel C, Tête MJ,

Montjean R, *et al.* (2011) INF2 mutations in Charcot-Marie-Tooth disease with glomerulopathy. *N Engl J Med* 365:2377–2388.

Breitsprecher D, Goode BL (2013) Formins at a glance. *J Cell Sci* 126:1–7.

Bucci C, Bakke O, Progida C (2012) Charcot-Marie-Tooth disease and intracellular traffic. *Prog Neurobiol* 99:191-225.

Cannon RC, Turner DA, Pyapali GK, Wheal HV (1998) An on-line archive of reconstructed hippocampal neurons. *J Neurosci Methods* 84:49–54.

Cassereau J, Chevrollier A, Gueguen N, Desquiret V, Verny C, Nicolas G, Dubas F, Amati-Bonneau P, Reynier P, Bonneau D, *et al.* (2011) Mitochondrial dysfunction and pathophysiology of Charcot-Marie-Tooth disease involving *GDAP1* mutations. *Exp Neurol* 227:31-41.

Chan DC (2006) Mitochondrial fusion and fission in mammals. *Annu Rev Cell Dev Biol* 22:79-99.

Chattopadhyay A, Gilstrap AV, Galko MJ (2012) Local and global methods of assessing thermal nociception in *Drosophila* larvae. *J Vis Exp* 63:e3837.

Chhabra ES, Higgs HN (2007) The many faces of actin: matching assembly factors with cellular structures. *Nat Cell Biol* 9:1110–1121.

Coles CH, Bradke F (2015) Coordinating neuronal actin-microtubule dynamics. *Curr Biol* 25:R677-R691.

Cuntz H, Forstner F, Borst A, Häusser M (2010) One rule to grow them all: A general theory of neuronal branching and its practical application. *PLoS Comput Biol* 6:e1000877

Das R, Bhattacharjee S, Patel AA, Harris JM, Bhattacharya S, Letcher JM, Clark SG, Nanda S, Iyer EPR, Ascoli GA, *et al.* (2017) Dendritic cytoskeletal architecture is modulated by combinatorial transcriptional regulation in *Drosophila melanogaster*. *Genetics* 207:1401-1421.

Detmer SA, Chan DC (2007) Functions and dysfunctions of mitochondrial dynamics. *Nat Rev Mol Cell Biol* 8:870-9.

Ekins S, Kitterman NK, Arnold RJG, Burgess RW, Freundlich JS, Gray SJ, Higgins JJ, Langley B, Willis DE, Notterpek L, *et al.* (2015) A brief review of recent Charcot-Marie-Tooth research and priorities. *F1000Research* 4:53.

Evangelista M, Pruyne D, Amberg DC, Boone C, Bretscher A (2002) Formins direct Arp2/3-independent actin filament assembly to polarize cell growth in yeast. *Nat Cell Biol* 4:32-41.

Feng L, Zhao T, Kim J (2015) neuTube 1.0: A new design for efficient neuron reconstruction software based on the SWC format. *eNeuro* 2:ENEURO.0049-14.2014.

Ferrandiz-Huertas C, Mathivanan S, Wolf CJ, Devesa I, Ferrer-Montiel A (2014) Trafficking of thermoTRP channels. *Membranes* 4:525-564.

Ferreira T, Blackman A, Oyrer J, Jayabal A, Chung A, Watt A, Sjöström J, van Meyel D (2014) Neuronal morphometry directly from bitmap images. *Nat Methods* 11(10):982–984.

Franker MAM, Hoogenraad CC (2013) Microtubule-based transport - basic mechanisms, traffic rules and role in neurological pathogenesis. *J Cell Sci* 126:2319–2329.

Gaillard J, Ramabhadran V, Neumann E, Gurel P, Blanchoin L, Vantard M, Higgs HN (2011) Differential interactions of the Formins INF2, mDia1, and mDia2 with microtubules. *Mol Biol Cell* 22:4575–4587.

Galbraith K, Kengaku M (2019) Multiple roles of the actin and microtubule-regulating formins in the developing brain. *Neurosci Res* 138:59-69.

Gasteier JE, Schroeder S, Muranyi W, Madrid R, Benichou S, Fackler OT (2005) FHOD1 coordinates actin filament and microtubule alignment to mediate cell elongation. *Exp Cell Res* 306:192–202.

Goode BL, Eck MJ (2007). Mechanism and function of Formins in the control of actin assembly. *Annu Rev Biochem* 76:593–627.

Goswami C (2012) TRPV1-tubulin complex: involvement of membrane tubulin in the regulation of chemotherapy-induced peripheral neuropathy. *J Neurochem* 123:1-13.

Goswami C, Hucho TB, Hucho F (2007) Identification and characterization of novel tubulin-binding motifs located within the C-terminus of TRPV1. *J Neurochem* 101:250-262.

Goswami C, Kuhn J, Dina OA, Fenandez-Ballester G, Levine JD, Ferrer-Montiel A, Hucho T (2011) Estrogen destabilizes microtubules through an ion-conductivity-independent TRPV1 pathway. *J Neurochem* 117:995-1008.

Halpain S, Dehmelt L (2006) The MAP1 family of microtubule-associate proteins. *Genome Biol* 7:224.

Herzmann S, Krumkamp R, Rode S, Kintrup C, Rumpf S (2017) PAR-1 promotes microtubule breakdown during dendrite pruning in *Drosophila*. *EMBO J* 36:1981-1991.

Higgs HN (2005) Formin proteins: A domain-based approach. *Trends Biochem Sci* 30:342–353.

Himmel NJ, Patel AA, Cox DN (2017) Invertebrate nociception. *Oxford Research Encyclopedia of Neuroscience*. Oxford University Press. doi:10.1093/acrefore/9780190264086.013.166

Himmel NJ, Letcher JM, Sakurai A, Gray TR, Benson MN, Cox DN (2019) *Drosophila* menthol sensitivity and the Precambrian origins of transient receptor potential-dependent chemosensation. *Phil Trans R Soc B* 374:20190369.

Hong E-H, Kim J-Y, Kim J-H, Lim D-S, Kim M, Kim J-Y (2018). BIG2-ARF1-RhoA-mDia1 signaling regulates dendritic Golgi polarization in hippocampal neurons. *Mol Neurobiol* 55:7701-7716.

Honjo K, Mauthner SE, Wang Y, Pate Skene JH, Tracey Jr. WD (2016) Nociceptor-enriched genes required for normal thermal nociception. *Cell Rep* 16:1-9.

Hummel T, Krukkert K, Roos J, Davis G, Klämbt C (2000) *Drosophila* Futsch/22C10 is a MAP1B-like protein required for dendritic and axonal development. *Neuron* 26:375-370.

Hwang RY, Zhong L, Xu Y, Johnson T, Zhang F, Deisseroth K, Tracey WD (2007) Nociceptive neurons protect *Drosophila* larvae from parasitoid wasps. *Curr Biol* 17:2105-2116.

Hwang RY, Stearns NA, Tracey WD (2012) The ankyrin repeat domain of the TRPA protein Painless is important for thermal nociception but not mechanical nociception. *PLoS ONE* 7(1):e30090.

Ishizaki T, Morishima Y, Okamoto M, Furuyashiki T, Kato T, Narumiya S (2001) Coordination of microtubules and the actin cytoskeleton by the Rho effector mDia1. *Nat Cell Biol* 3:8-14.

Iyer EPR, Iyer SC, Sullivan L, Wang D, Meduri R, Graybeal LL, Cox DN (2013) Functional genomic analyses of two morphologically distinct classes of *Drosophila* sensory neurons: Post-mitotic roles of transcription factors in dendritic patterning. *PLoS ONE* 8:e72434.

Jonchere V, Bennett D (2013) Validating RNAi phenotypes in *Drosophila* using a synthetic RNAi-resistant transgene. *PLoS ONE* 8:e70489.

Kapitein LC, Hoogenraad CC (2015). Building the neuronal microtubule cytoskeleton. *Neuron* 87:492-506.

Korobova F, Ramabhadran V, Higgs HN (2013) An actin-dependent step in mitochondrial fission mediated by the ER-associated formin INF2. *Science* 339:464-467.

Kovar DR (2006) Molecular details of Formin-mediated actin assembly. *Curr Opin Cell Biol* 18:11-17.

Lainez S, Valente P, Ontoria-Oviedo I, Estevez-Herrera J, Camprubi-Robles M, Ferrer-Montiel A, Planells-Cases R (2010) GABAA receptor associated protein (GABARAP) modulates TRPV1 expression and channel function and desensitization. *FASEB J* 24:1958-1970.

Landouré G, Zdebik AA, Martinez TL, Burnett BG, Stanescu HC, Inada H, Shi Y, Taye AA, Kong L, Munns CH, *et al.* (2010) Mutations in TRPV4 cause Charcot-Marie-Tooth disease type 2C. *Nat Genet* 42:170-204.

Lefebvre JL, Sanes JR, Kay JN (2015) Development of dendritic form and function. *Annu Rev Cell Dev Biol* 31:741-777.

Li F, Higgs HN (2003) The mouse Formin mDia1 is a potent actin nucleation factor regulated by autoinhibition. *Curr Biol* 13:1335–1340.

Lopez-Bellido R, Himmel NJ, Gutstein HB, Cox DN, Galko MJ (2019) An assay for chemical nociception in *Drosophila* larvae. *Phil Trans R Soc B* 374:20190282.

López-Doménech G, Higgs NF, Vaccaro V, Roš H, Arancibia-Cárcamo IL, MacAskill AF, Kittler JT (2016) Loss of dendritic complexity precedes neurodegeneration in a mouse model with disrupted mitochondrial distribution in mature dendrites. *Cell Rep* 17:317-327.

Nanda S, Das R, Cox DN, Ascoli GA (2017) Structural plasticity in dendrites: developmental neurogenetics, morphological reconstructions, and computational modeling. In: *Neurobiological and Psychological Aspects of Brain Recovery* (Petrosini, L, ed), pp1-34 Springer Press, Contemporary Clinical Neuroscience Series: Cham.

Nanda S, Bhattacharjee S, Cox DN, Ascoli GA (2020) Distinct relations of microtubules and actin filaments with dendritic architecture. *iScience* 23:101865.

Nanda S, Chen H, Das R, Bhattacharjee S, Cuntz H, Torben-Nielsen B, Peng H, Cox DN, De Schutter E, Ascoli GA (2018) Design and implementation of multi-signal and time-varying neural reconstructions. *Sci Data* 5:170207.

Niehues S, Bussman J, Steffes G, Erdmann I, Kohrer C, Sun L, Wagner M, Schafer K, Wang G, Koerdts SN, *et al.* (2014) Impaired protein translation in *Drosophila* models for Charcot-Marie-Tooth neuropathy caused by mutant tRNA synthetases. *Nat Commun* 6:7520.

Ori-McKenney KM, Jan LY, Jan YN (2012) Golgi outposts shape dendrite morphology by functioning as sites of acentrosomal microtubule nucleation in neurons. *Neuron* 76:921–930.

Peng H, Bria A, Zhou Z, Iannello G, Long F (2014) Extensible visualization and analysis for multidimensional images using Vaa3D. *Nat Protoc* 9:193–208.

Qu X, Yuan FN, Corona C, Pasini S, Pero ME, Gundersen GG, Shelanski ML, Bartolini F (2017) Stabilization of dynamic microtubules by mDia1 drives Tau-dependent A β 1-42 synaptotoxicity. *J Cell Biol* 216:3161-3178.

Ramabhadran V, Korobova F, Rahme GJ, Higgs HN (2011) Splice variant-specific cellular function of the Formin INF2 in maintenance of Golgi architecture. *Mol Biol Cell* 22:4822–4833.

Rolls MM (2011) Neuronal polarity in *Drosophila*: sorting out axons and dendrites. *Dev Neurobiol* 71:419-429.

Rolls MM, Satoh D, Clyne PJ, Henner AL, Uemura T, Doe CQ (2007) Polarity and intracellular compartmentalization of *Drosophila* neurons. *Neural Dev* 2(1):7.

Roos J, Hummel T, Ng N, Klämbt C, Davis GW (2000) *Drosophila* Futsch regulates synaptic microtubule organization and is necessary for synaptic growth. *Neuron* 26:371-382.

Rosales-Nieves AE, Johndrow JE, Keller LC, Magie CR, Pinto-Santini DM, Parkhurst SM. (2006) Coordination of microtubule and microfilament dynamics by *Drosophila* Rho1, Spire and Cappuccino. *Nat Cell Biol* 8:367–376.

Roth-Johnson EA, Vizcarra CL, Bois JS, Quinlan ME (2014) Interaction between microtubules and the *Drosophila* Formin Cappuccino and its effect on actin assembly. *J Biol Chem* 289:4395–4404.

Schindelin J, Arganda-Carreras I, Frise E, Kaynig V, Longair M, Pietzsch S, Rueden C, Saalfeld S, Schmid B, Tinevez JY *et al.* (2012) Fiji: an open-source platform for biological-image analysis. *Nat Methods* 9:676–682.

Schulz JG, David G, Hassan BA (2009) A novel method for tissue-specific RNAi rescue in *Drosophila*. *Nucl Acids Res* 37(13):e93.

Shaye DD, Greenwald I (2015) The disease-associated Formin INF2/EXC-6 organizes lumen and cell outgrowth during tubulogenesis by regulating F-Actin and microtubule cytoskeletons. *Dev Cell* 32:743–755.

Storti B, Bizzarri R, Cardarelli F, Beltram F (2012) Intact microtubules preserve transient receptor potential vanilloid 1 (TRPV1) functionality through receptor binding. *J Biol Chem* 287:7803-7811.

Sulkowski MJ, Iyer SC, Kurosawa MS, Iyer EPR, Cox DN (2011) Turtle functions downstream of Cut in differentially regulating class specific dendrite morphogenesis in *Drosophila*. *PLoS ONE* 6:e22611.

Tanaka H, Takasu E, Algaki T, Kato K, Hayashi S, Nose A (2004) Formin3 is required for assembly of the F-actin structure that mediates tracheal fusion in *Drosophila*. *Dev Biol* 274:413-425.

Tao J, Feng C, Rolls MM (2016) The microtubule-severing protein fidgetin acts after dendrite injury to promote their degeneration. *J Cell Sci* 129:3274-3281.

Thurston SF, Kulacz WA, Shaikh S, Lee JM, Copeland JW (2012) The ability to induce microtubule acetylation is a general feature of Formin proteins. *PLoS ONE* 7:e48041.

Tracey WD, Wilson RI, Laurent G, Benzer S. *painless*, a *Drosophila* gene essential for nociception (2003) *Cell* 113:261–273.

Tsubouchi A, Tsuyama T, Fujioka M, Kohda H, Okamoto-Furuta, K, Aigaki T, Uemura T (2009) Mitochondrial protein Preli-like is required for development of dendritic arbors and prevents their regression in the *Drosophila* sensory nervous system. *Development* 136:3757-3766.

Tsuyama T, Tsubouchi A, Usui T, Imamura H, Uemura, T (2017) Mitochondrial dysfunction induces dendritic loss via eIF2a phosphorylation. *J Cell Biol* 216:815-834.

Wearne SL, Rodriguez A, Ehlenberger DB, Rocher AB, Henderson SC, Hof PR (2005) New techniques for imaging, digitization and analysis of three-dimensional neural morphology on multiple scales. *Neuroscience* 136:661-680.

Ye B, Petritsch C, Clark IE, Gavis ER, Jan LY, Jan YN (2004) *nanos* and *pumilio* are essential for dendrite morphogenesis in *Drosophila* peripheral neurons. *Curr Biol* 14:314-321.

Ye B, Zhang Y, Song W, Younger SH, Jan LY, Jan YN (2007) Growing dendrites and axons differ in their reliance on the secretory pathway. *Cell* 130:717-729.

Zhang W, Cheng LE, Kittlemann M, Li J, Petkovic M, Cheng T, Jin P, Guo Z, Göpfert MC, Jan LY *et al.* (2015) Ankyrin repeats convey force to gate the NOMPC mechanotransduction channel. *Cell* 162:1391-1403.

Zhong L, Bellemer A, Yan H, Ken H, Jessica R, Hwang RY, Pitt GS, Tracey WD (2012) Thermosensory and nonthermosensory isoforms of *Drosophila melanogaster* TRPA1 reveal heat-sensor domains of a thermoTRP Channel. *Cell Rep* 1:43-55.

Zuchner S, Mersiyanova IV, Muglia M, Bissar-Tadmouri N, Rochelle J, Dadali EL, Zappia M, Nelis E, Patitucci A, Senderek J, *et al.* (2004) Mutations in the mitochondrial GTPase mitofusin 2 cause Charcot-Marie-Tooth neuropathy type 2A. *Nat Genet* 36:449-451.

Figures

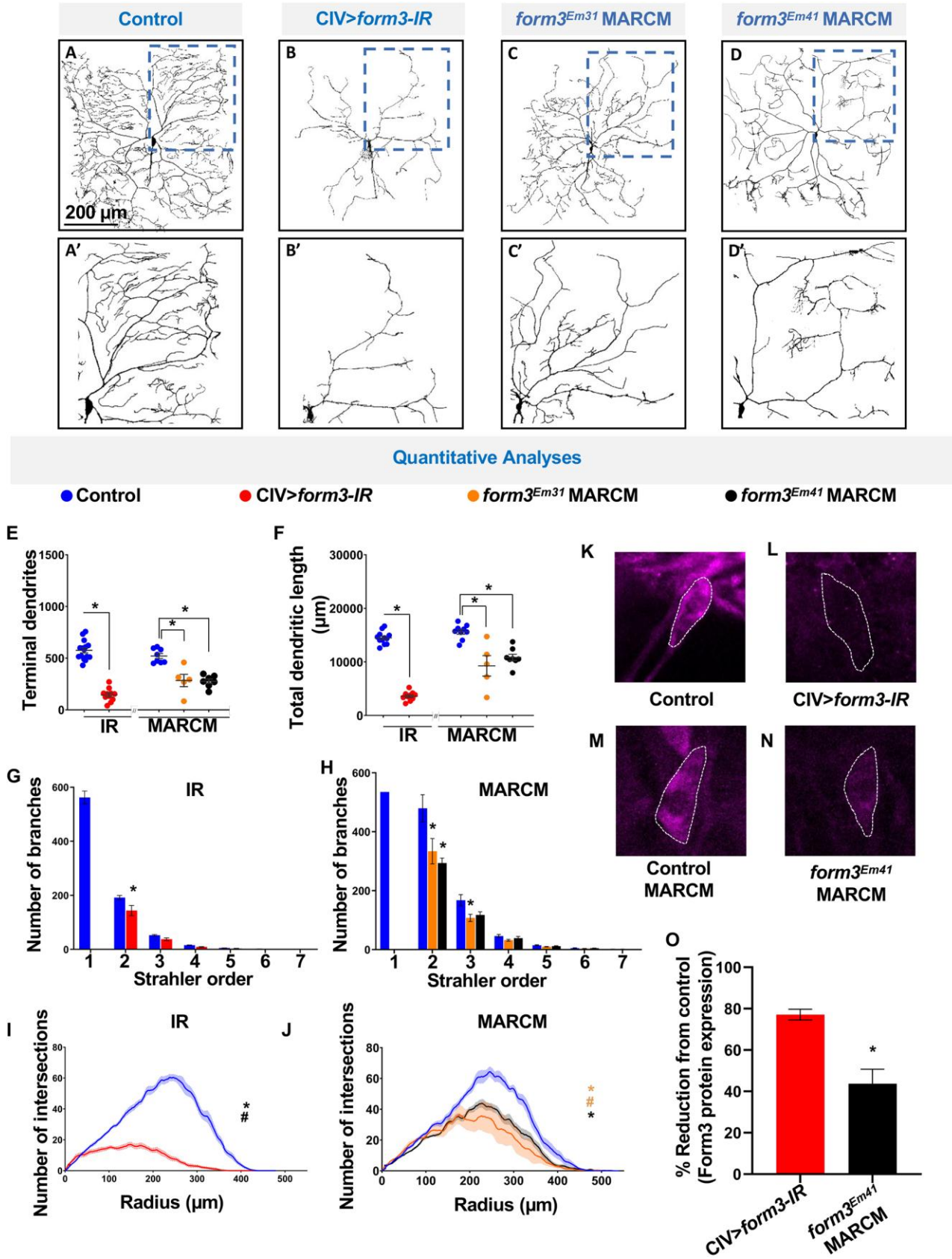


Figure 1: *form3* is required for dendritic growth and higher order branching complexity.

Representative images of dendritic arbors of CIV (ddaC) neurons in (A) control (N=12), (B) *form3-IR* (IR) (N=10), (C) *form3^{Em31}* MARCM (N=5), and (D) *form3^{Em41}* MARCM (N=8). (A'-D') Enlarged insets indicated in (A-D). (E,F) Quantitative dendritic analyses. Values are the mean \pm SEM. (G,H) Reverse Strahler analysis of control vs. *form3-IR* (G) and MARCM (H). Values are the mean \pm SEM for number of dendritic branches in each branch order (Strahler order) where 7=primary branch from cell body and 1=terminal branch. (I,J) Sholl profile of control vs. *form3-IR* (I) and MARCM (J). Values are the mean \pm SEM for number of intersections as a function of radial distance from the cell body (zero). (K-N) IHC labeling against Form3 protein in (K) CIV control, (L) CIV>*form3-IR*, (M) CIV control MARCM, and (N) *form3^{Em41}* MARCM 3rd instar larvae. (O) Quantification of % reduction in Form3 expression in CIV>*form3-IR* (N=14) vs. *form3^{Em41}* MARCM (N=8) relative to controls. Statistical test performed: (E_{IR}) unpaired t-test p=0.0001, (E_{MARCM}) one-way ANOVA with Bonferroni correction p=0.0005 (Em31) and p=0.0011 (Em41); (F_{IR}) unpaired t-test p=0.00001, (F_{MARCM}) one-way ANOVA with Bonferroni correction p=0.0003 (Em31) and p=0.0011 (Em41); (G,H) two-way ANOVA with Bonferroni correction: (G₂) p=0.005; (H_{2-Em31,Em41}) p=0.0001, (H_{3-Em31}) p=0.0307; (I) unpaired t-test for critical value (*) and the corresponding radius (#) p=0.0001 for both parameters. (J) one-way ANOVA with Bonferroni correction for critical value (*) and corresponding radius (#), p=0.0001 (orange, Em31 *), p=0.0029 (orange, Em31 #), p=0.0001 (black, Em41 *), p>0.05 (black, Em41 #); (O) Mann-Whitney U test p<0.0001. See also Figure S1 and Figure S2.

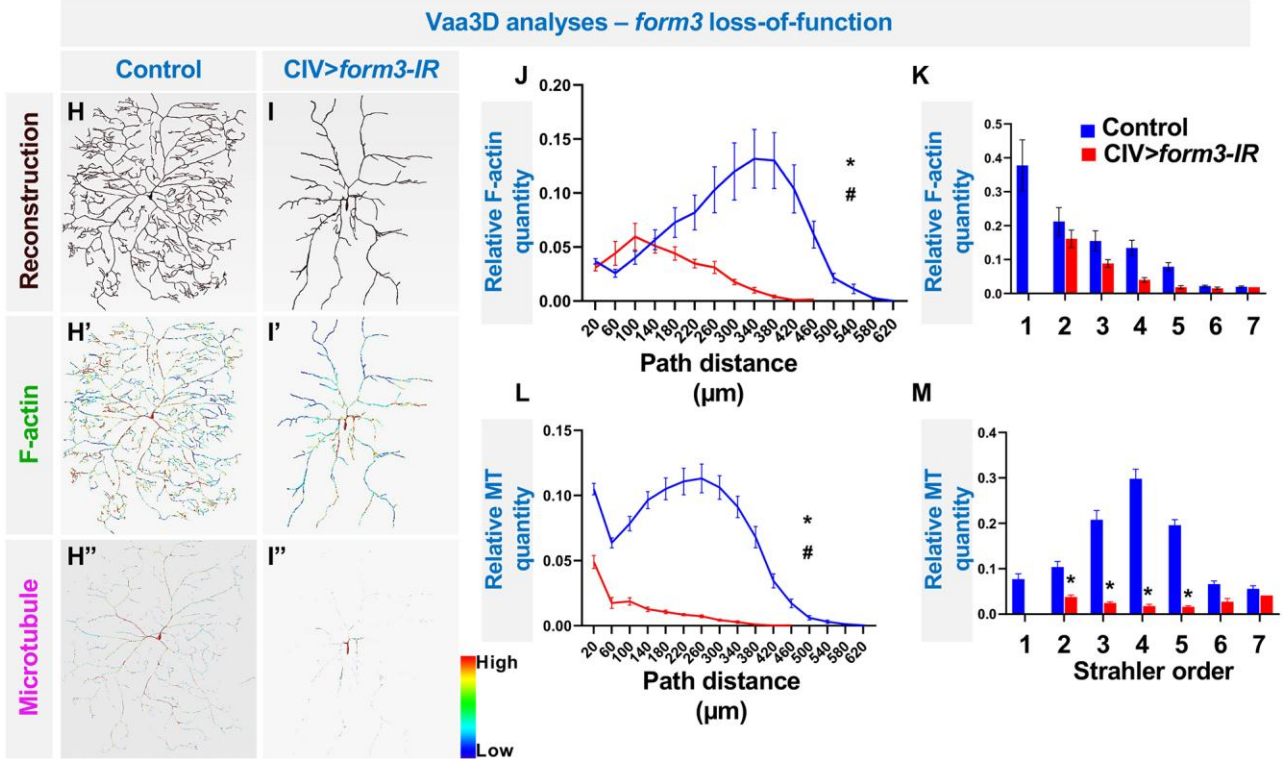
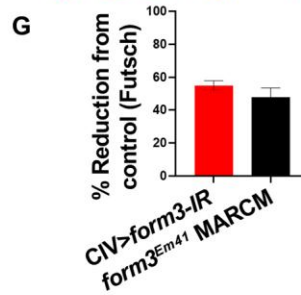
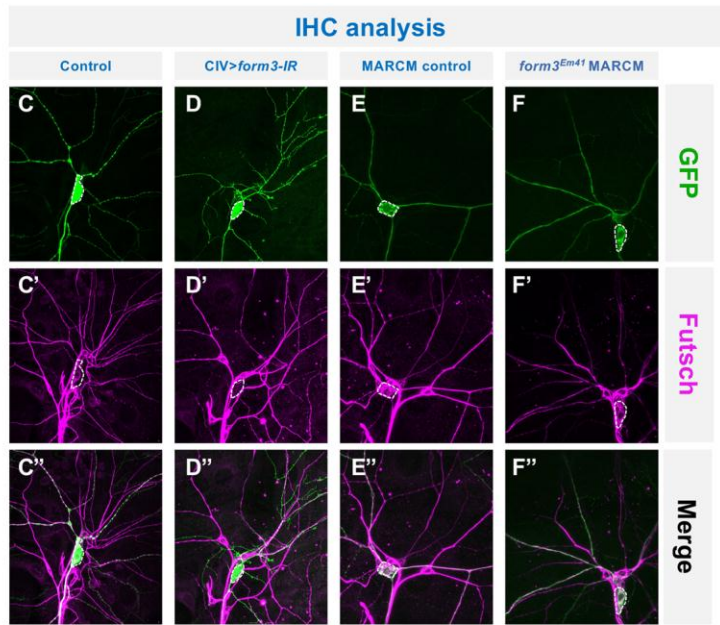
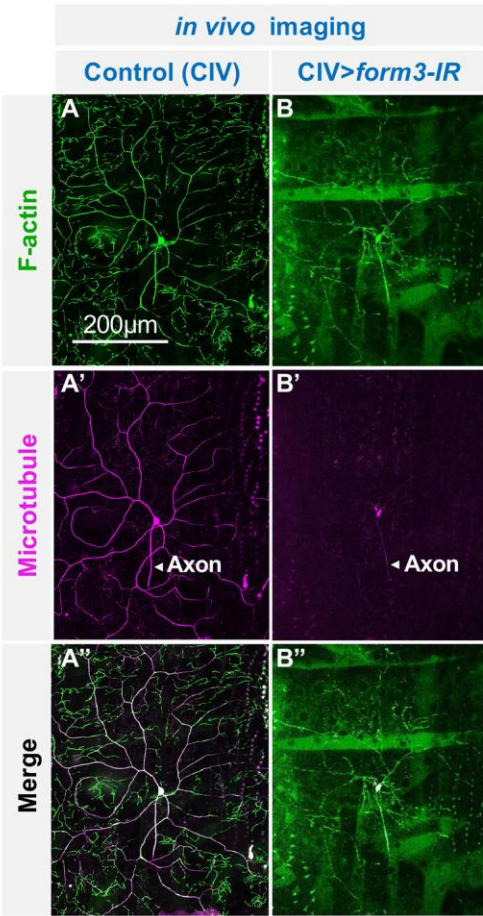


Figure 2: *form3* functions in F-actin organization and microtubule stabilization.

(A-B'') CIV-*GAL4*-driven expression of *UAS-GMA* (which labels F-actin filaments via a GFP fused to the Moesin actin binding domain) and *UAS-mCherry::Jupiter* (which labels MTs via an mCherry fused to the MAP molecule Jupiter). (A-A'') Control CIV neuron. (B-B'') *form3-IR* CIV neuron reveals disruption of F-actin organization and dendritic stable MTs. Representative images of N=10 CIV neurons per genotype. (C-F'') IHC of third instar larval filets double labeled with antibodies to GFP (C-F) and the MAP1B protein Futsch (C'-F') in (C) CIV control, (D) CIV>*form3-IR*, (E) MARCM control, and (F) *form3^{Em41}* MARCM. CI (ddaD/E) and CIII (ddaF) neurons exhibit normal, strong Futsch expression on MTs. Representative images of dorsal da neuron clusters. (G) Quantification of % reduction in Futsch staining in CIV>*form3-IR* (N=7) vs. *form3^{Em41}* MARCM (N=10) relative to controls. (H-I) Representative skeletal reconstructions of control and *form3-IR* CIV neurons, generated by a combination of Vaa3D, Neutube, and TREES Toolbox. (H',H'',I',I'') Intensity maps of F-actin and MT generated in Vaa3D (N=5 per genotype). (J,L) Relative subcellular distributions of F-actin and MTs as a function of path distance from the soma; values are the mean \pm SEM. (K,M) Relative F-actin and MT quantity by Strahler order distribution, where 7=primary branch from cell body and 1=terminal branch; values are the mean \pm SEM. Statistical test performed: (G) Mann-Whitney *U* test, $p > 0.05$; (J) unpaired t-test for critical value (*) $p = 0.0191$ and corresponding radius (#) $p = 0.00005$; (L) unpaired t-test for critical value (*) $p = 0.0060$ and corresponding radius (#) $p = 0.000443$. (K,M) two-way ANOVA with Bonferroni correction: (K₂) $p = 0.0035$, (K₃) $p = 0.0043$; (M_{3,4,5}) $p = 0.0001$, (M₇) $p = 0.0055$.

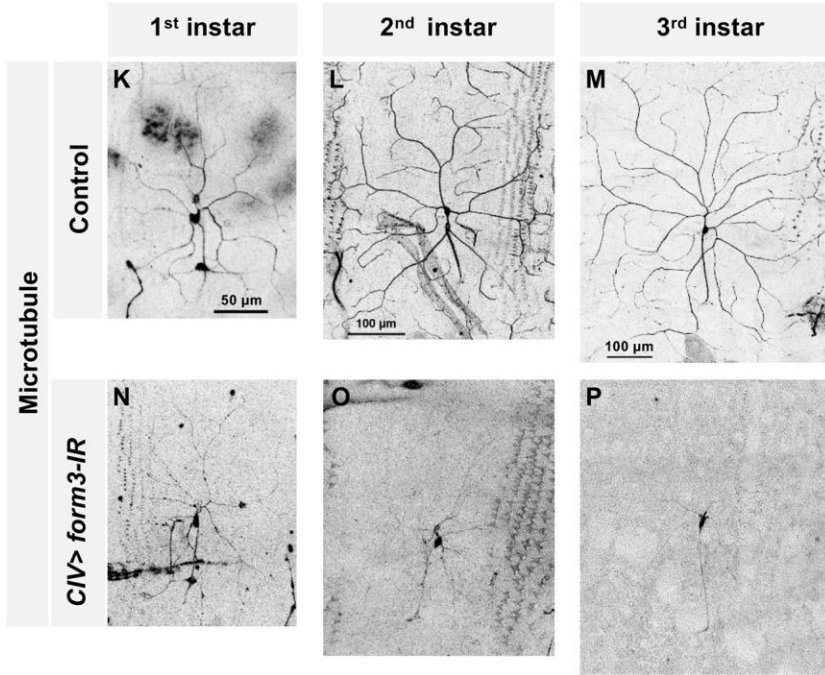
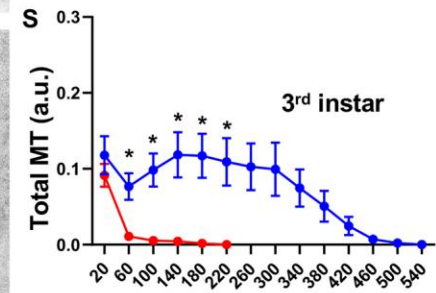
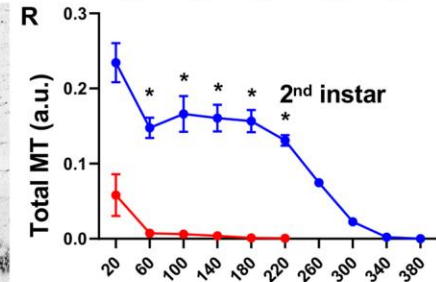
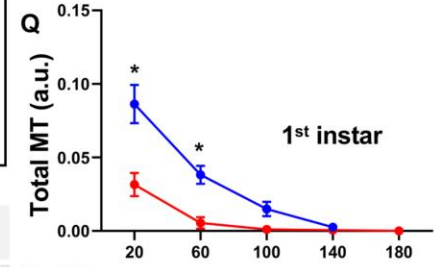
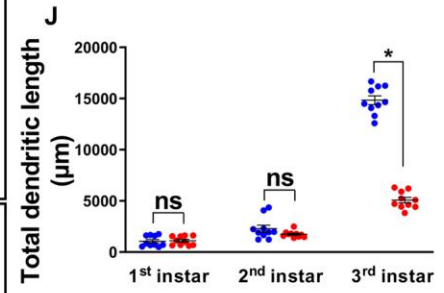
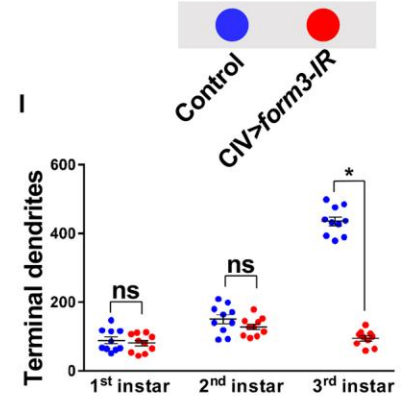
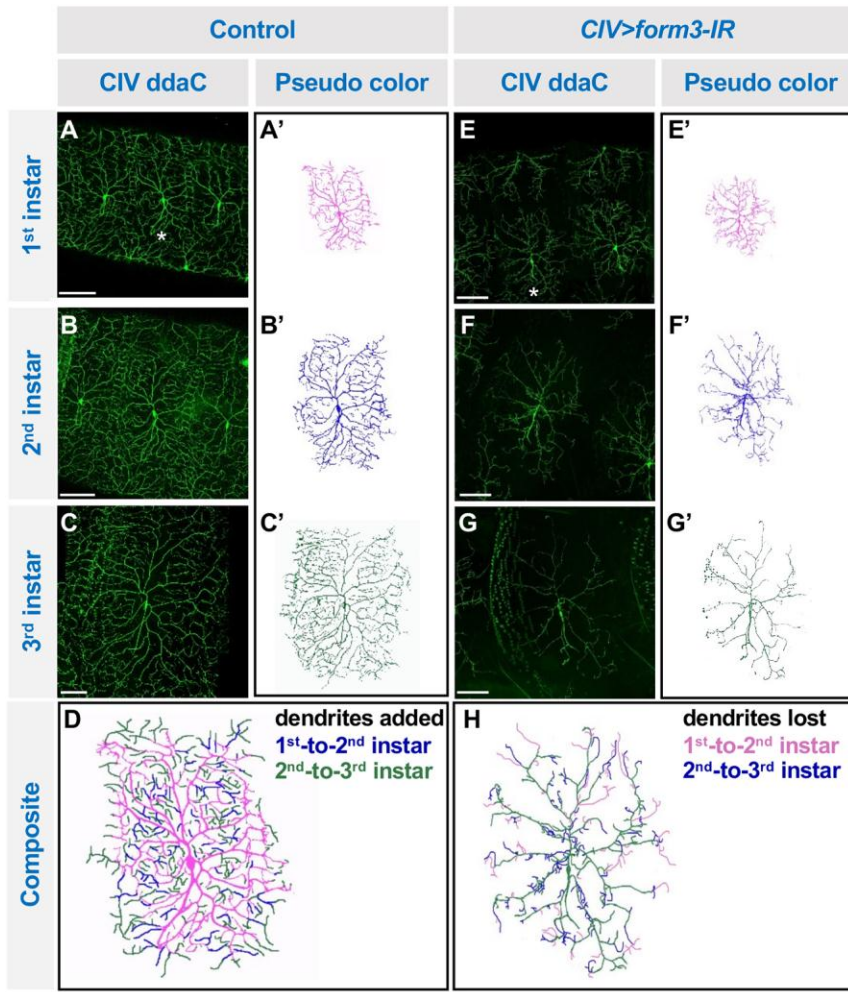


Figure 3: *form3* is required for dendritic arbor maintenance. (A-H) Representative larval developmental time course images of the same CIV neuron taken of control (A,B,C) and *form3-IR* (E,F,G) at 1st, 2nd, and 3rd instar larval stages, respectively. (A'-C'; E'-G') Pseudo-colored panels show the same neuron color coded for its developmental stages (magenta as 1st, blue as 2nd, and green as 3rd instar). (D) Composite image shows the arborization of dendritic branches that occurred from 1st to 2nd to 3rd instar stages, where blue marks those dendrites added from 1st to 2nd instar, and green marks those dendrites that were added from 2nd to 3rd instar. (H) Composite image shows the loss of the dendritic branches that occurred from 1st to 2nd to 3rd instar stages, where magenta marks those dendrites that were lost from 1st to 2nd instar, and blue marks those dendrites lost from 2nd to 3rd instar. Note, in panels D and H the branches are not exactly to scale. (I,J) Quantitative analyses of the number of branches and total dendritic length of control (N=10) and *form3-IR* (N=10) CIV neurons at different stages of development as indicated on the figure. Error bars represent mean \pm SEM. (K-P) CIV-*GAL4*-driven expression of *UAS-mCherry::Jupiter* in control (N=9) (K-M) or *form3-IR* (N=8) (N-P) at different stages of development as indicated on the figure. (Q-S) Relative distribution of MTs as a function of path distance from soma. Values are the mean \pm SEM. Statistical test performed: (I,J) unpaired t-test, (I_{3rd-instar}) p=0.0001; (J_{3rd-instar}) p=0.0001. ns represents not significant p>0.05; (Q-S) two-way ANOVA with Bonferroni correction *=p<0.05, (R,S) MTs beyond 220 μ m from the soma in *form3-IR* were not detected. See also Figure S3.

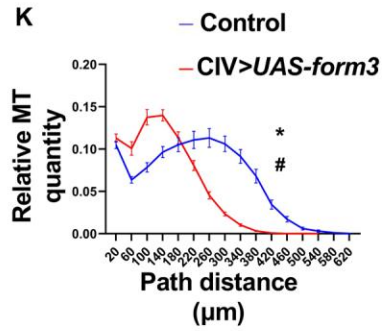
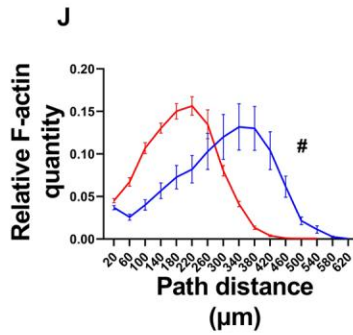
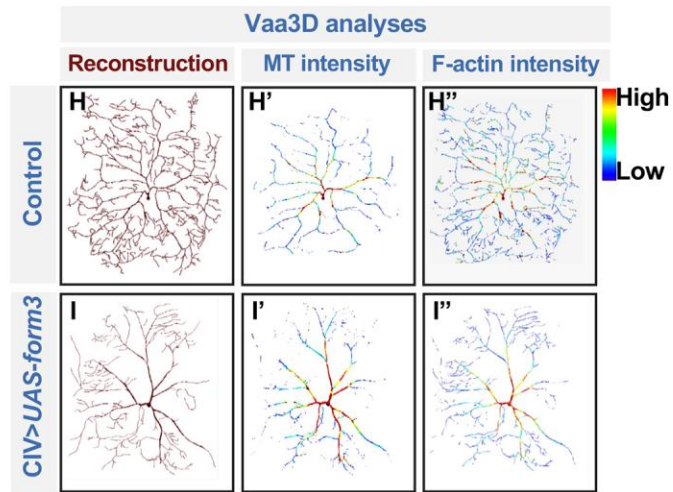
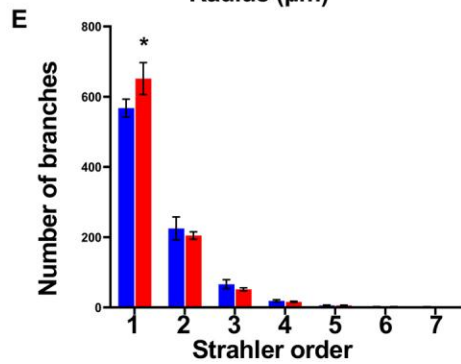
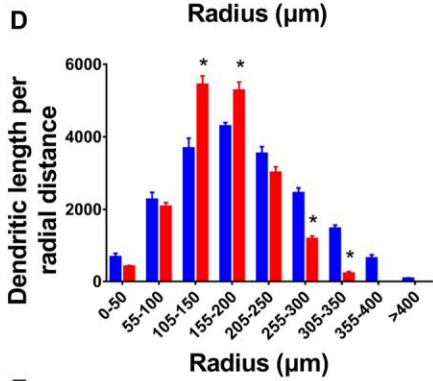
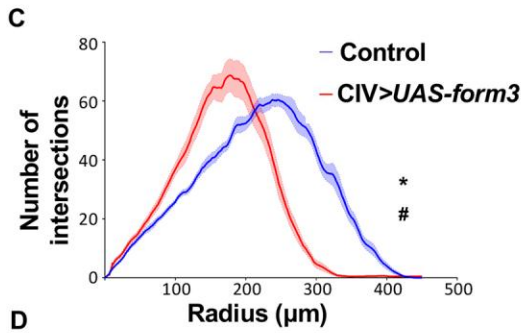
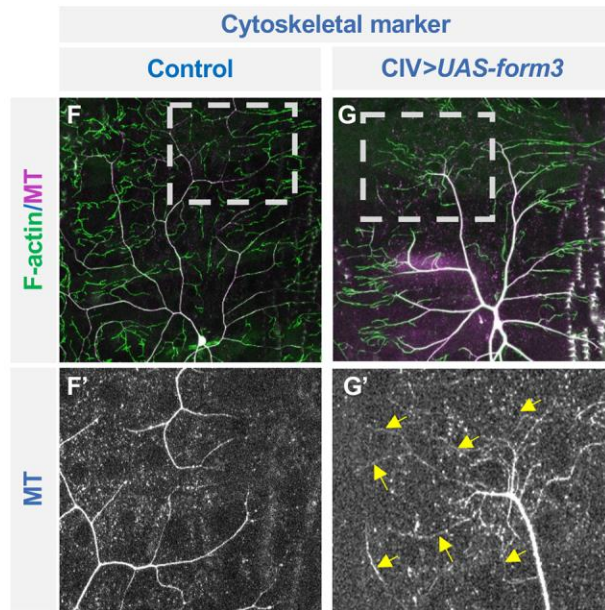
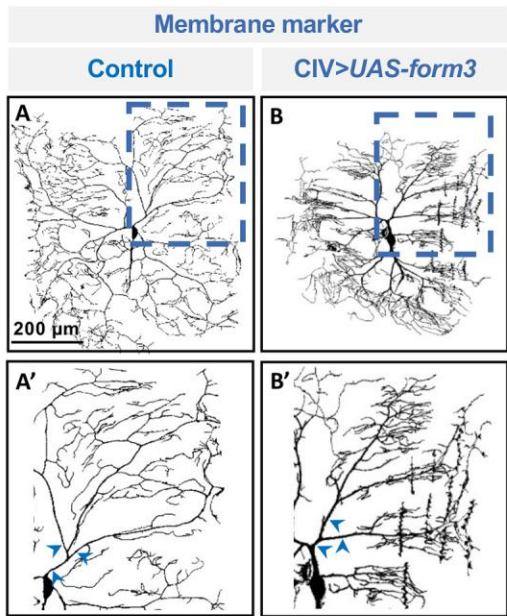
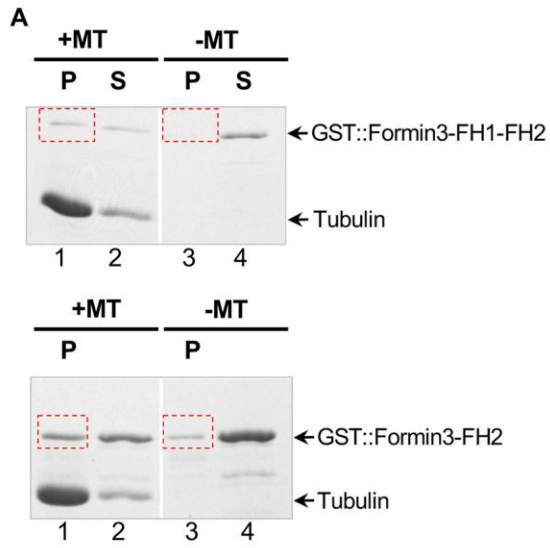


Figure 4: Form3 overexpression promotes higher order terminal branching and shifts branch and cytoskeletal distributions. (A,A') Representative image of control CIV neurons (N=12). (B,B') Representative image of *form3* overexpression CIV neurons (N=7). Relative to controls (A,A'), *form3* overexpression (B,B') leads to a distal shift in branching complexity characterized by excessive growth of terminal dendritic branches and thickened lower order (e.g. primary, secondary) branches, indicated by blue arrowheads. (C,D) Sholl profile of control (N=12) vs. *form3* overexpression (N=7). Values are the mean (\pm SEM) for the number of intersections as a function of radius distance from the cell body (zero). (D) Sholl profiles for control vs. *form3* overexpression data plotted as histogram to reflect the total number of intersections per corresponding radial distance (Euclidean) from the soma (zero) to the terminals highlighting local effects on branch distributions. (E) Reverse Strahler analysis of control vs. *form3* overexpression. Values are the mean (\pm SEM) for the number of dendritic branches in each branch order (Strahler order), where 7=primary branch from cell body and 1=terminal branch. (F,F') Dendritic terminals of control CIV neurons (N=10) are rich in F-actin processes. (G,G') Dendritic terminals of CIV neurons overexpressing Form3 (N=10) are populated by F-actin processes, but also display increased MT invasion into these processes. (H-I') Multichannel reconstructions of cytoskeletal features in control (N=5) and *form3* overexpression (N=8) CIV neurons. Heat maps represent the relative distribution and intensity of F-actin and MTs in controls vs. *form3* overexpression. Note that *form3* overexpression leads to increased MT intensity and abnormally increased diameters of primary dendritic branches. (J,K) Relative subcellular distributions of F-actin and MTs as a function of path distance from the soma. Statistical test performed: (C) unpaired t-test for critical value (*) $p=0.00825$ and the corresponding radius (#) $p=0.00041$; (D,E) two-way ANOVA with Bonferroni correction: (D₁₀₅₋₁₅₀) $p=0.0001$, (D₁₅₅₋₂₀₀) $p=0.0005$; (D₂₅₅₋₃₀₀) $p<0.0001$; (D₃₀₅₋₃₅₀) $p=0.0001$, (E₁) $p=0.0001$; (J) unpaired t-test for corresponding radius (#) $p=0.002528$; (K) unpaired t-test for critical value (*) $p=0.024318$ and for corresponding radius (#) $p=0.000419$. Data are represented as mean \pm SEM. See also Figure S4.

MT binding co-sedimentation assay



MT precipitation assay

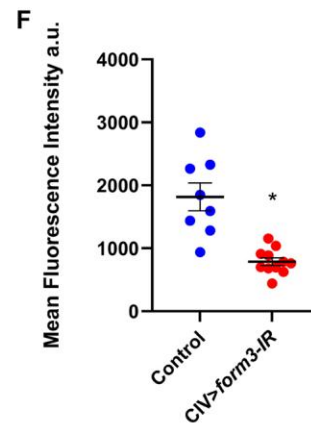
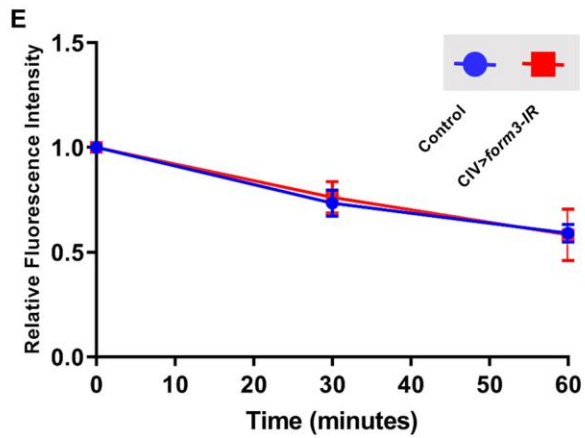
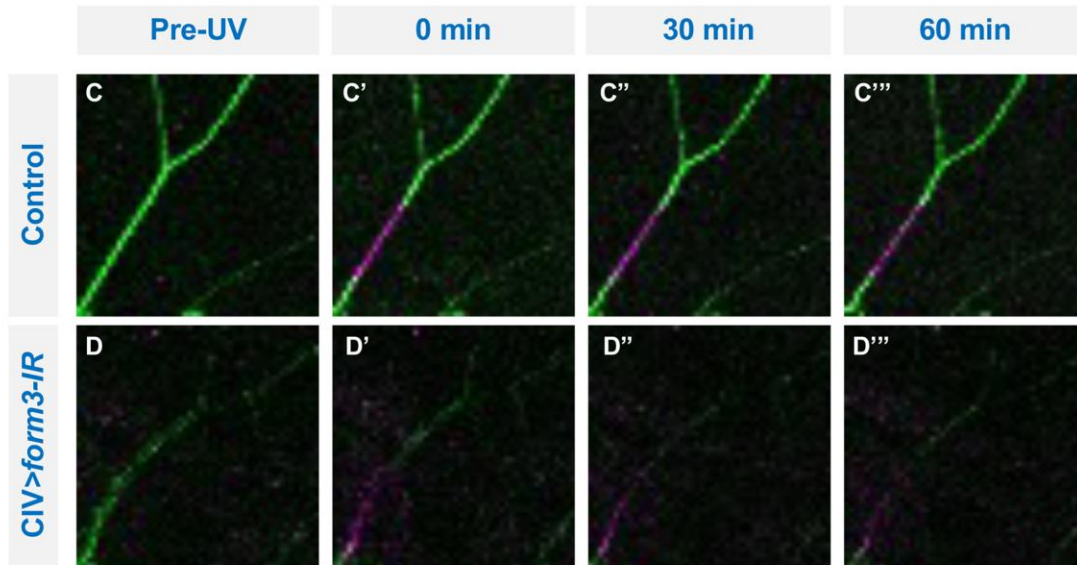
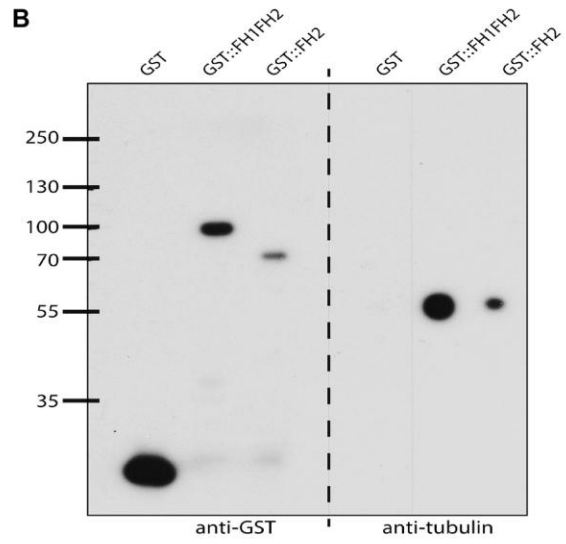
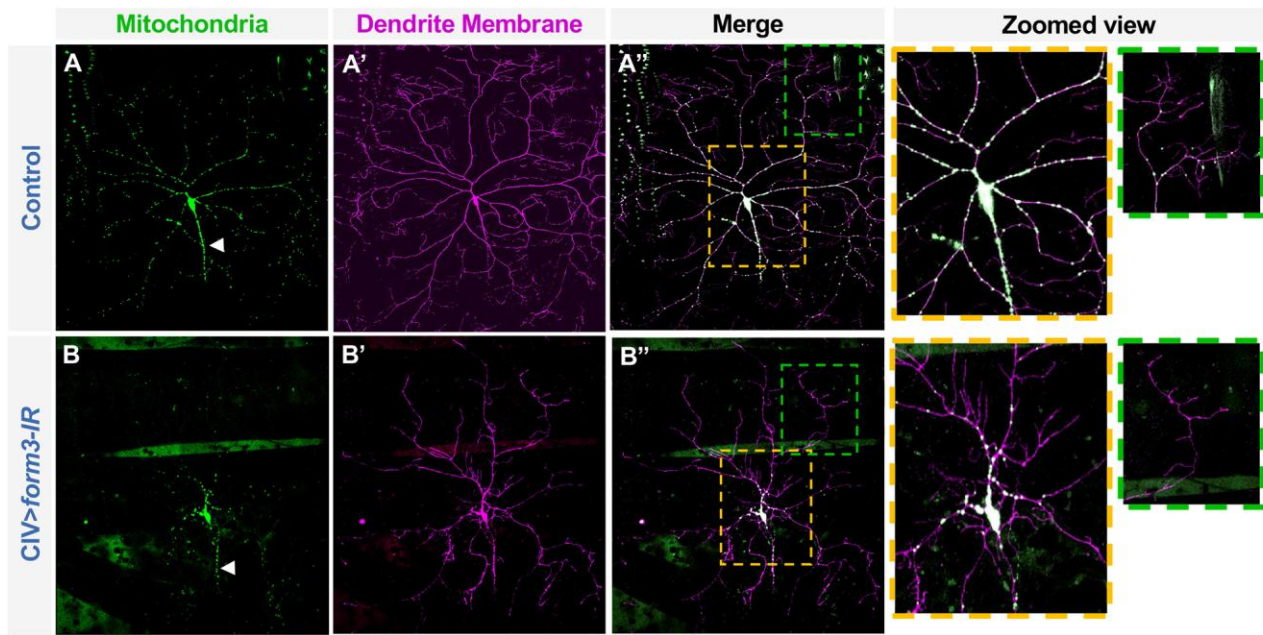


Figure 5: *form3* interacts directly with microtubules. (A) MT co-sedimentation assay. GST-tagged Form3 constructs expressing either the FH1-FH2 domains or the FH2 domain alone incubated in the presence or absence of MTs. Western blots probed for anti-GST and anti- α -tubulin. The FH1-FH2 fusion displays specific co-sedimentation in pellet fractions only in the presence of MTs, whereas the FH2 fusion displays a low level of self-pelleting that is notably increased in the presence of MTs. Pellet fractions indicated by dashed red boxes, P=pellet, S=supernatant. (B) MT precipitation assay. Western blots probed for anti-GST or anti- α -tubulin. Tubulin co-precipitates only in the presence of the Form3 GST fusion constructs, but not with the GST construct alone. Protein molecular weights indicated at left in kDa. Biochemical assays performed in duplicate. (C-D'') Time-lapse imaging of MT turnover. *form3-IR* (N=11) animals (D-D'',E) show a similar rate of MT turnover to that of controls (N=8) (C-C'',E) for the subpopulation of MTs that remain in *form3*-depleted neurons. However, *form3-IR* animals have less initial MT as compared to controls (F). Statistical test performed: (E) Unpaired t-test at 0, 30, and 60 minutes, not significant $p>0.05$; (F) Unpaired t-test, $p=0.000085$. See also Figure S5.



◁ Axon *ppk::tdTomato*; CIV>GAL4, *UAS-mito-HA-GFP.AP*

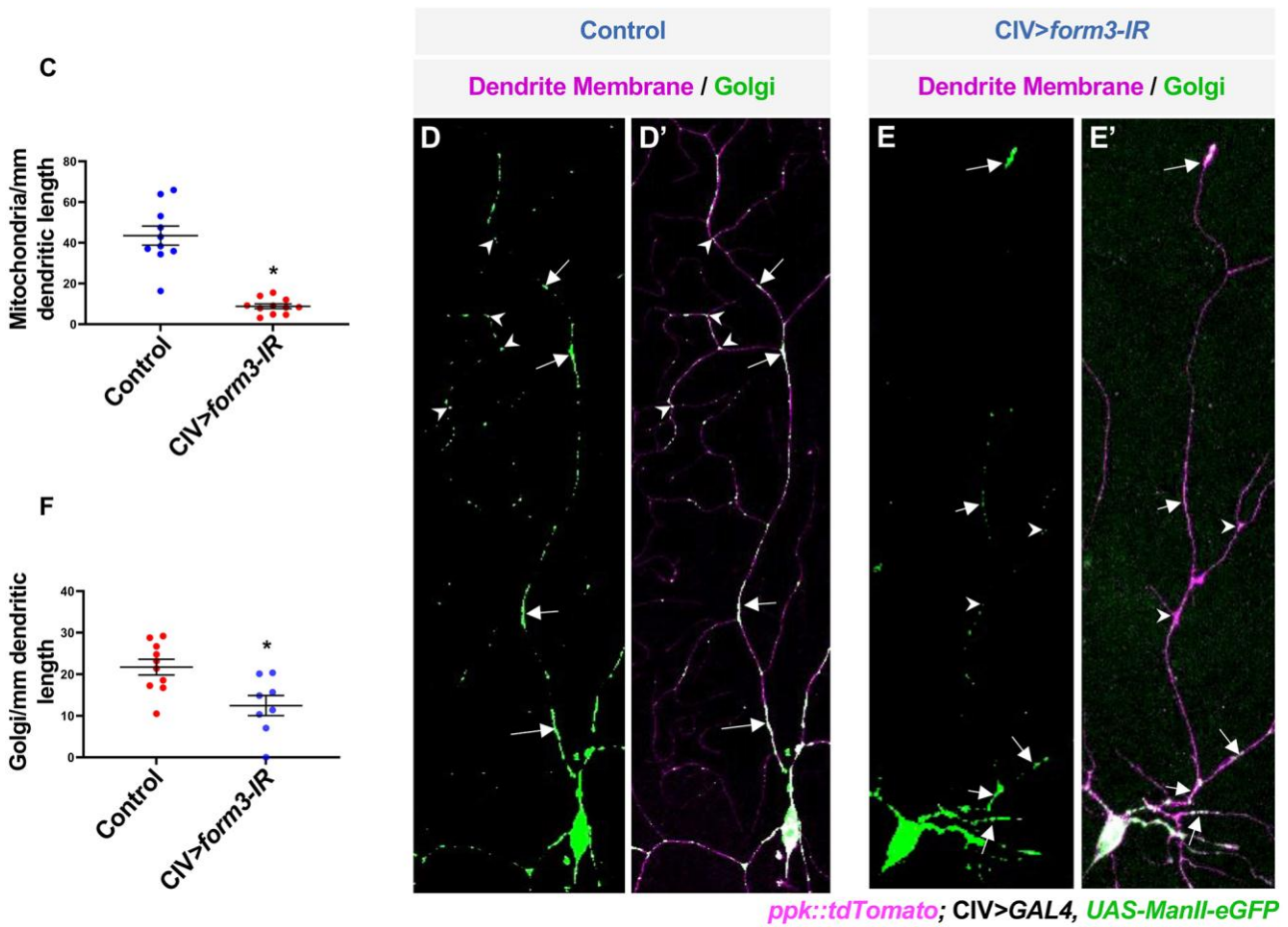


Figure 6: *form3* is required for dendritic organelle localization. Relative to controls (N=10) (**A-A''**), *form3-IR* (N=11) CIV neurons (**B-B''**) exhibit dendritic collapse (**B'**) and a severe mitochondrial mislocalization within dendrites (**B,B''**), but not proximal axons (arrowheads). Zoomed view of the corresponding colored boxes, where orange box represents an area proximal to the cell body and green box represents an area distal to the cell body. (**C**) Fewer dendritic mitochondria are present in *form3-IR* neurons (N=10) relative to controls (N=11). Relative to controls (N=5) (**D-D'**), *form3-IR* (N=6) CIV neurons (**E-E'**) exhibit defects in dendritic Golgi localization and aberrant Golgi architecture (**E'**). (**D-E'**) Arrows denote locations of interstitial “islands” of fused Golgi (control) or punctate Golgi (*form3-IR*); arrowheads denote dendritic branch points. (**F**) Fewer Golgi outposts are present in *form3-IR* neurons (N=10) relative to controls (N=10). Statistical test performed: (**C,F**) unpaired t-test, $p < 0.01$.

A

H. sapiens INF2

D. melanogaster Form3

INF2 Rescue Transgenes

Full length INF2

FH1-FH2 only

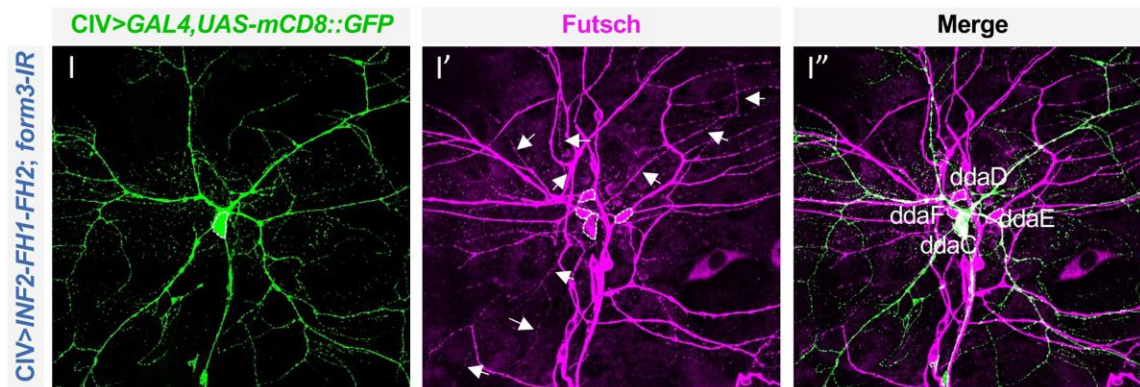
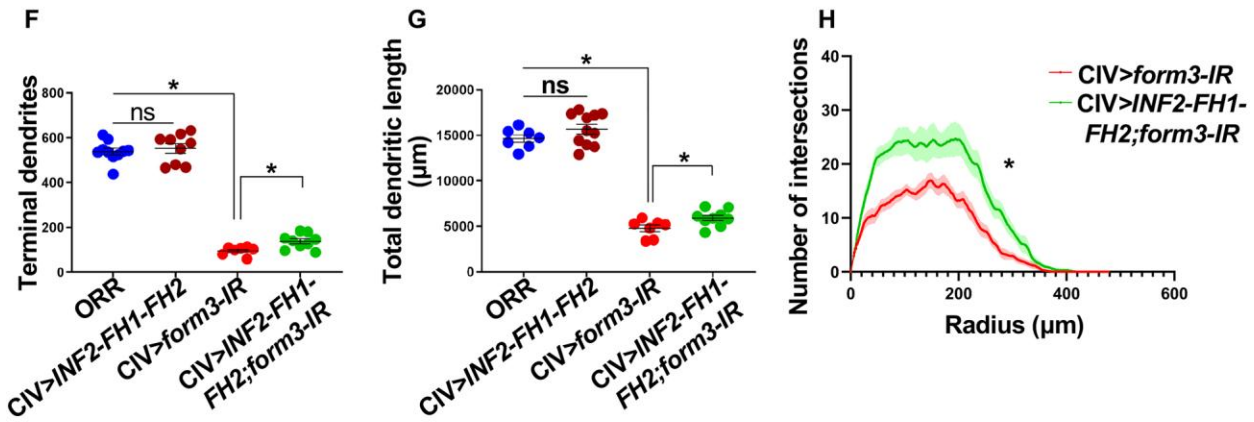
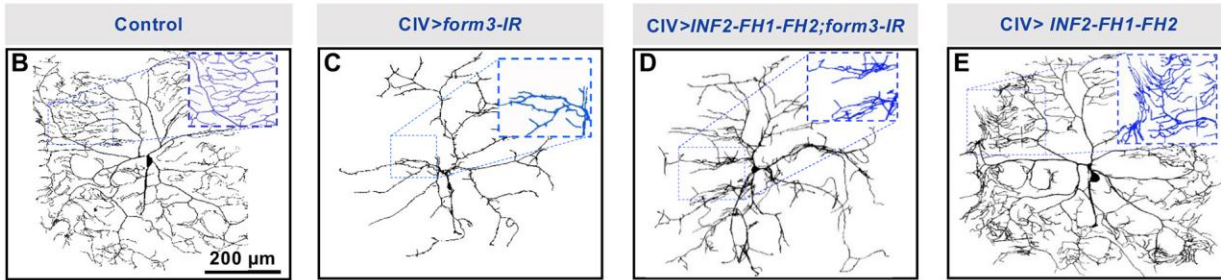
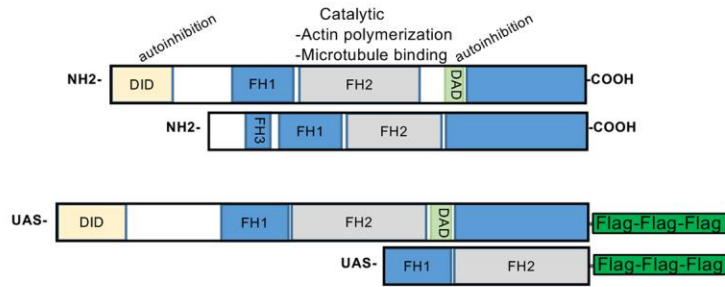


Figure 7: *INF2* can partially alleviate *form3* depletion defects in dendrite complexity and stable MTs.

(A) Schematic diagrams of human *INF2* and *Drosophila* *Form3* domain organization; schematic diagrams of *INF2* rescue transgenes. (B) Control CIV neurons (N=7). (C) CIV-*form3-IR* (N=7). (D) CIV-specific expression of *form3-IR* with simultaneous expression of *INF2-FH1-FH2* in the same neuron (N=9). (E) CIV-specific expression of *INF2-FH1-FH2* (N=11). (F,G) Quantitative measurements of number of terminal branches and total dendritic length (error bars represent SEM). (H) Sholl critical radius for indicated genotypes. (I-I'') CIV-specific expression of *INF2-FH1-FH2* in *form3-IR* background (N=8). Introduction of *INF2-FH1-FH2* partially recovers MT signal on cell body and dendrites of CIV neurons as labeled with anti-Futsch (magenta). Arrows in panel I' depict labeling of CIV dendrite MTs. Statistical test performed: (F) Mann-Whitney *U* test $p > 0.05$ (ORR vs. *INF2-FH1-FH2*), $p = 0.003$ (ORR vs. *form3-IR*), $p = 0.0003$ (*form3-IR* vs *INF2-FH1-FH2;form3-IR*); (G) Mann-Whitney *U* test $p > 0.05$ (ORR vs. *INF2-FH1-FH2*), $p = 0.0003$ (ORR vs. *form3-IR*), $p = 0.0209$ (*form3-IR* vs. *INF2-FH1-FH2;form3-IR*). (H) unpaired t-test $p = 0.0083$. See also Figure S6.

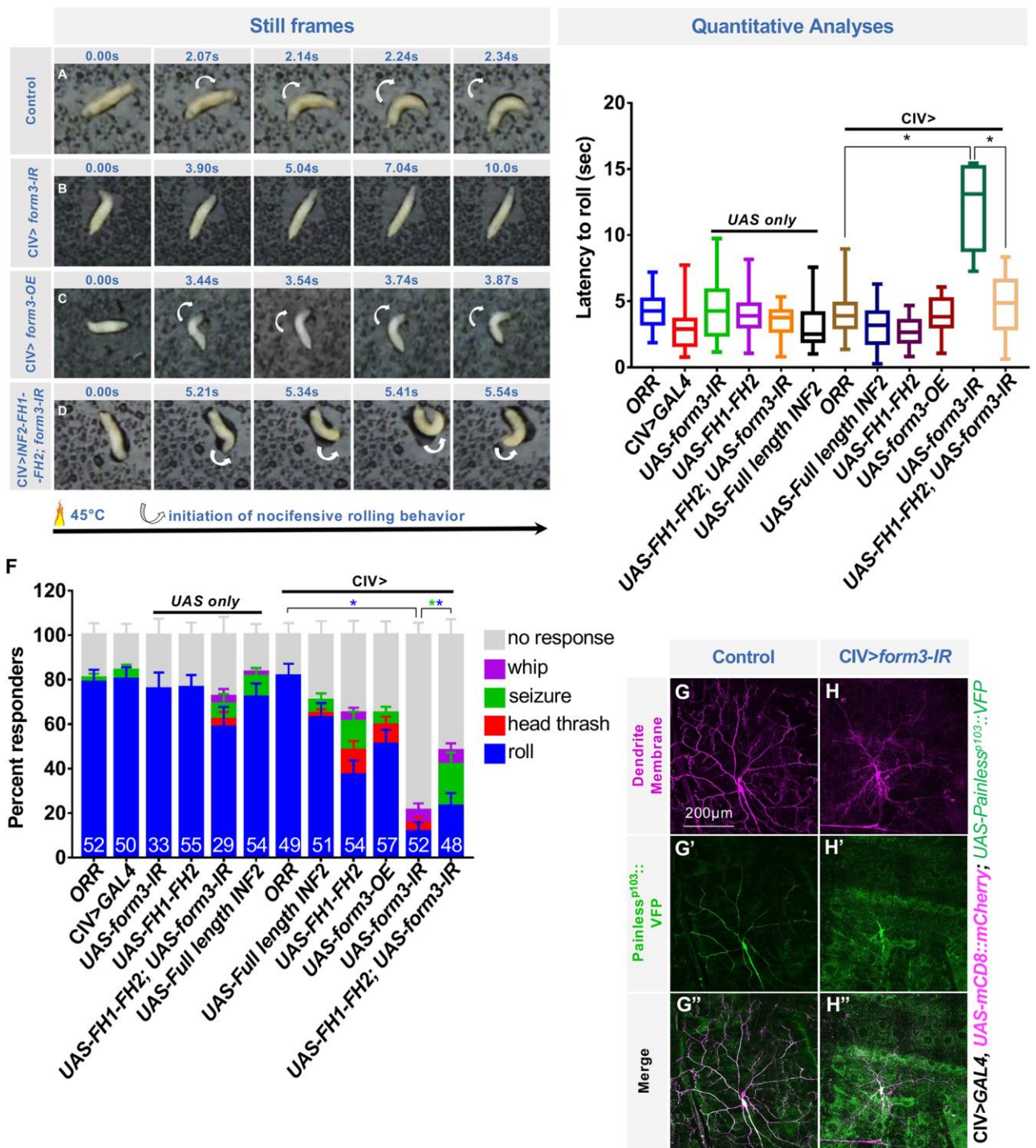


Figure 8: *form3* is required for noxious heat nociception, which can be rescued by introduction of *INF2-FH1-FH2*. (A-D) Representative still images of noxious heat-evoked rolling behavior for the designated genotypes. (E) Latency to roll in seconds (mean ± SEM) for the designated genotypes at 45°C. (F) Percent responders (mean ± SEP) for the respective nocifensive behaviors in the designated genotypes at 45°C. Number of third instar larvae (N) for (E,F) by genotype is represented on

the bar graph displayed in (F). (G-H") Representative images of the CIV-specific expression of *UAS-painless^{p103}::VFP* in control (N=10) or *form3-IR* (N=7) neurons, where dendrite membrane is labeled with *UAS-mCD8::mCherry* in magenta (G,H) and *painless^{p103}::VFP* in green (G',H'). Statistical test performed: (E) one-way ANOVA with Bonferroni correction; comparisons are indicated on the figure. (E) p=0.0001 (CIV>*UAS-form3-IR*) and p=0.0001 (CIV>*UAS-FH1-FH2;UAS-form3*). (F) Fisher's exact test with Bonferroni correction p=0.0001 (CIV>*UAS-form3-IR*) and p=0.00001 (CIV>*UAS-FH1-FH2;UAS-form3-IR* for roll) and p=0.00001 (CIV>*UAS-FH1-FH2;UAS-form3-IR* for seizure).

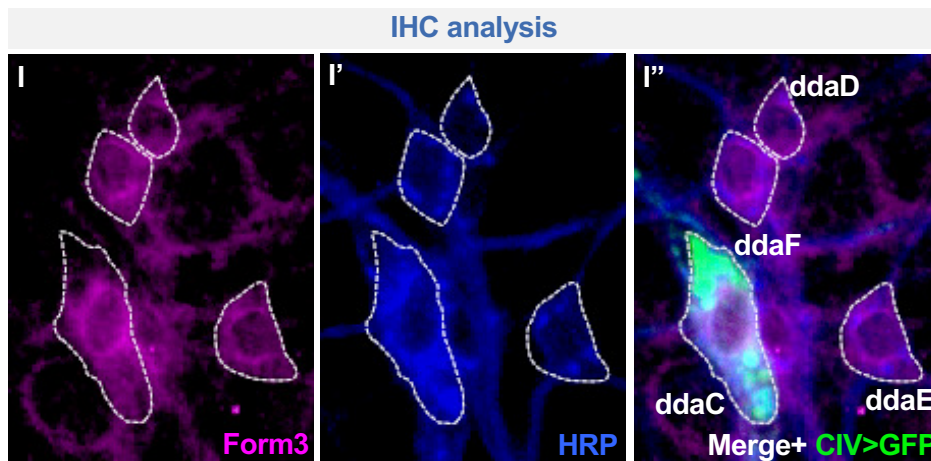
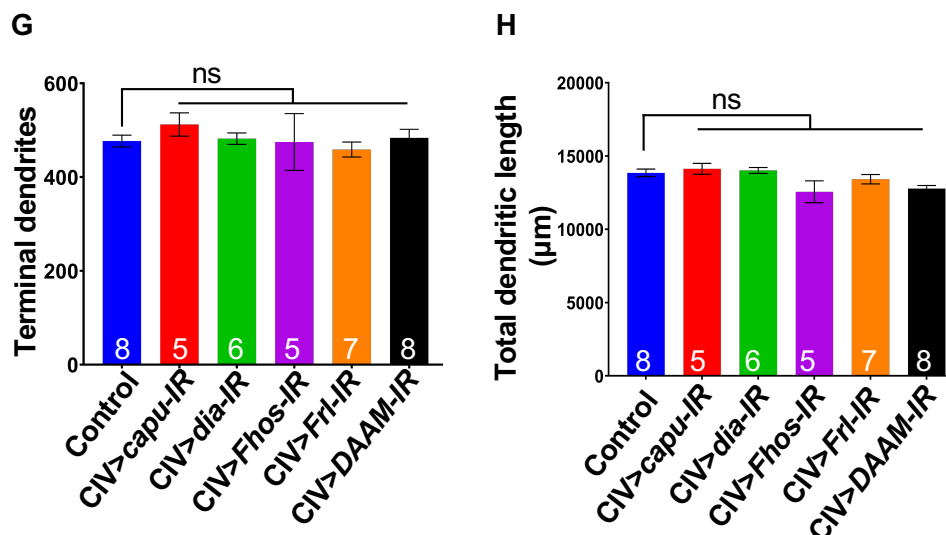
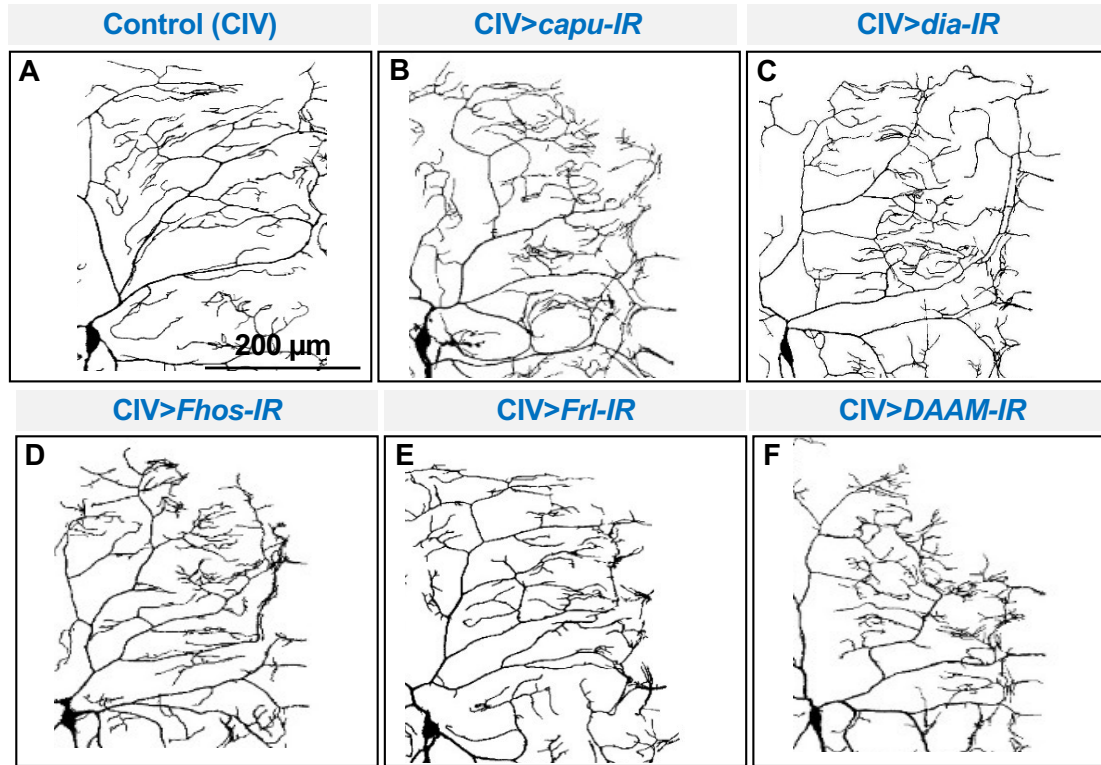


Fig. S1. Phenotypic analyses of *Drosophila Formins*. (A-F) Representative images of CIV dendrites in (A) control and (B-F) RNAi knockdowns for *Drosophila Formins* *capu*, *dia*, *Fhos*, *Frl*, and *DAAM*. (G,H) Quantitative neuromorphometric analyses (mean \pm SEM) with N value indicated on the graphs. (I-I'') CIV-specific GAL4477,UAS-mCD8::GFP third instar larval filets triple labeled with (I) Form3, (I') HRP, and (I'') Merge+GFP. Representative image of N=8 dorsal da neuron clusters. Statistical test performed (G,H): one-way ANOVA with Bonferroni correction; ns represents not significant $p > 0.05$.

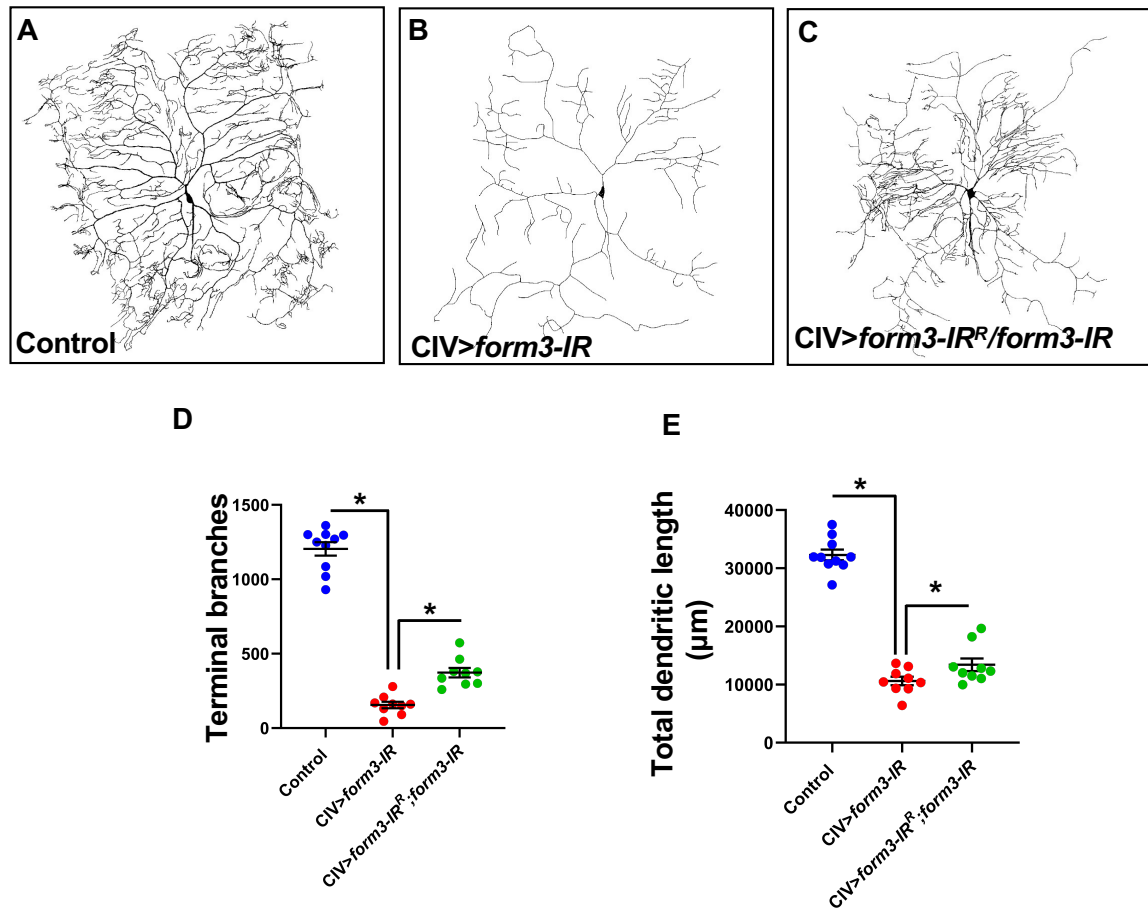


Fig. S2. Co-expression of RNAi-resistant *form3* and *form3-IR* partially rescues *form3-IR*-induced dendritic defects. (A-C) Representative images of CIV neurons in (A) control, (B) *form3-IR*, and (C) *form3-IR^R;form3-IR*. (D,E) Quantitative analyses of the terminal branches and total dendritic length of control (N=11), *form3-IR* (N=10), and *form3-IR^R;form3-IR* (N=10) CIV neurons. Statistical tests performed: (D) unpaired t-test $p < 0.0001$ (control vs. *form3-IR* and *form3-IR* vs. *form3-IR^R;form3-IR*); (E) unpaired t-test $p < 0.0001$ (control vs. *form3-IR*); Mann-Whitney *U* test $p < 0.05$ (*form3-IR* vs. *form3-IR^R;form3-IR*).

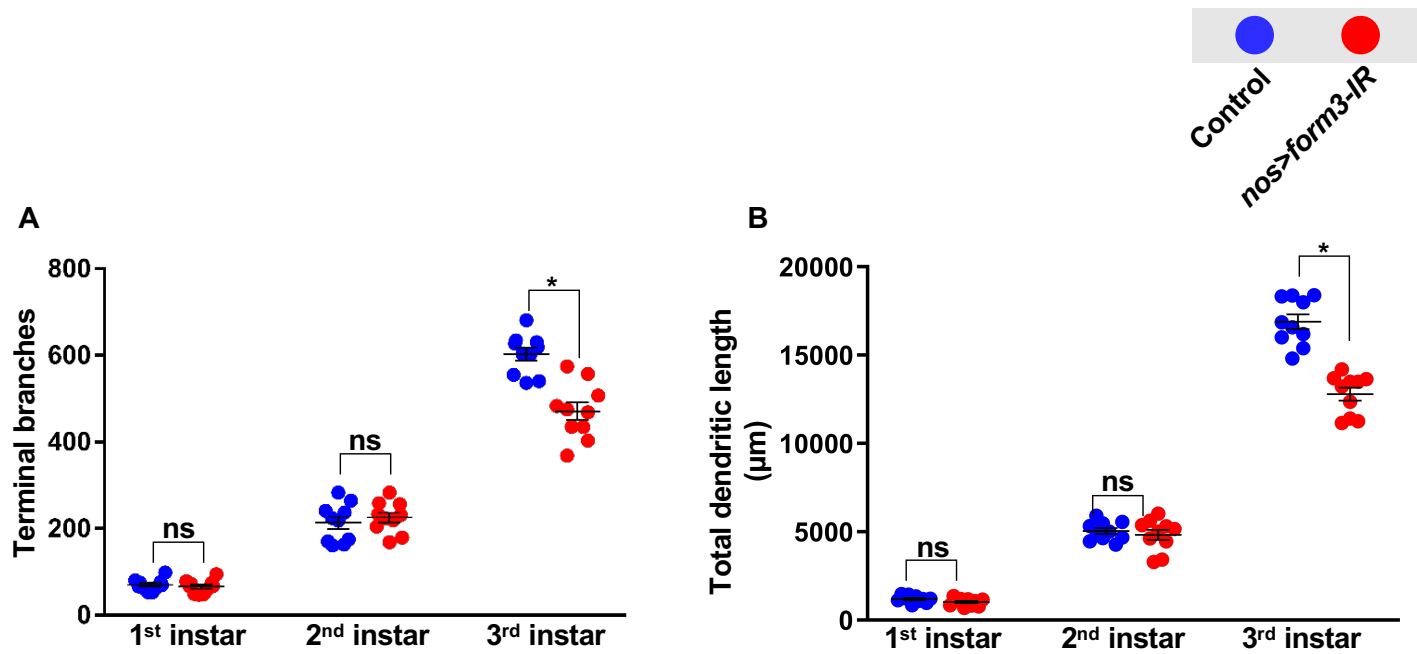


Fig. S3. *Form3* is required to maintain higher order dendritic branching over developmental time.

(A,B) Quantitative analyses of the number of branches (A) and total dendritic length (B) of control (N=10) and *nos-GAL4>form3-IR* (N=10) at different stages of development as indicated on the figure. Statistical test performed: (A,B) unpaired t-test, (A_{3rd-instar}) and (B_{3rd-instar}) $p < 0.0001$. ns represents not significant $p > 0.05$. Error bars indicate SEM.

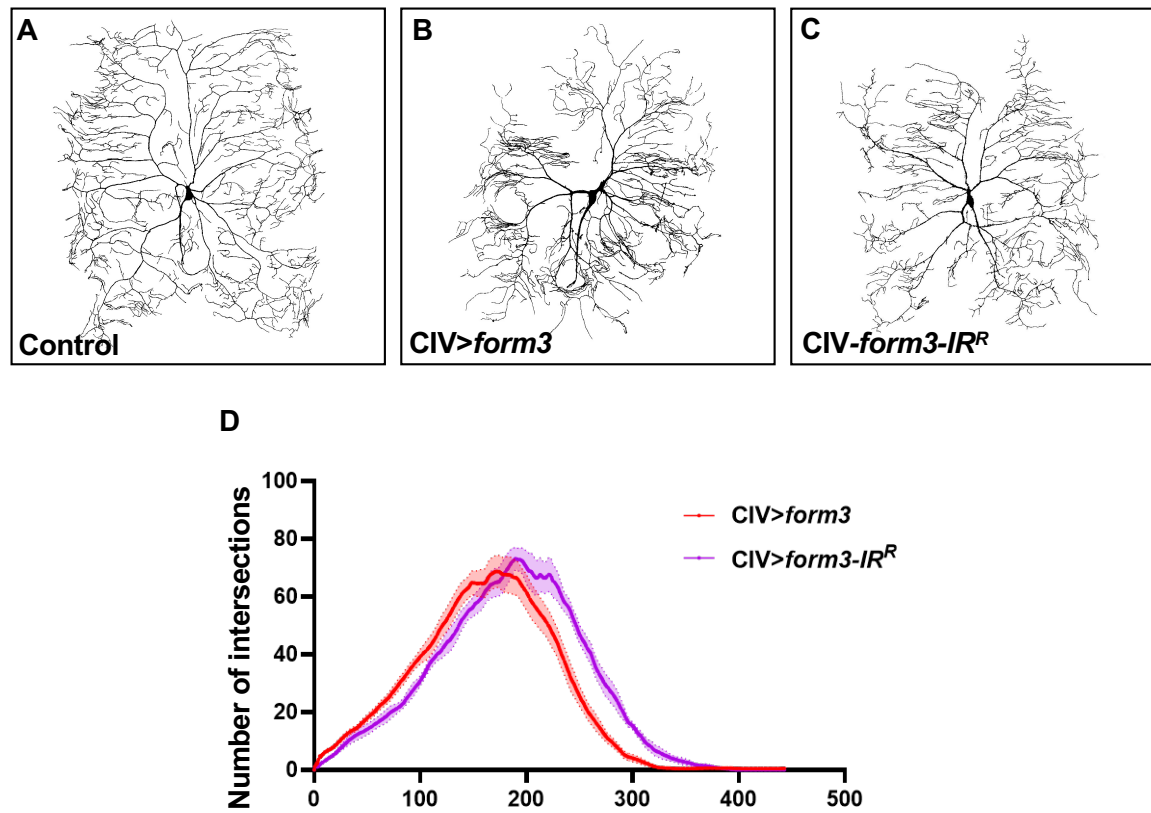


Fig. S4. Overexpression of *form3* RNAi resistant transgene. (A-C) Representative images of CIV neurons in (A) control, (B) *form3* overexpression, and (C) *form3-IR^R* overexpression. (D) Sholl profile of control (N=11), *form3* (N=11), and *form3-IR^R* (N=5). Statistical tests performed: (D) unpaired t-test $p > 0.05$, not significant for critical value or radius.

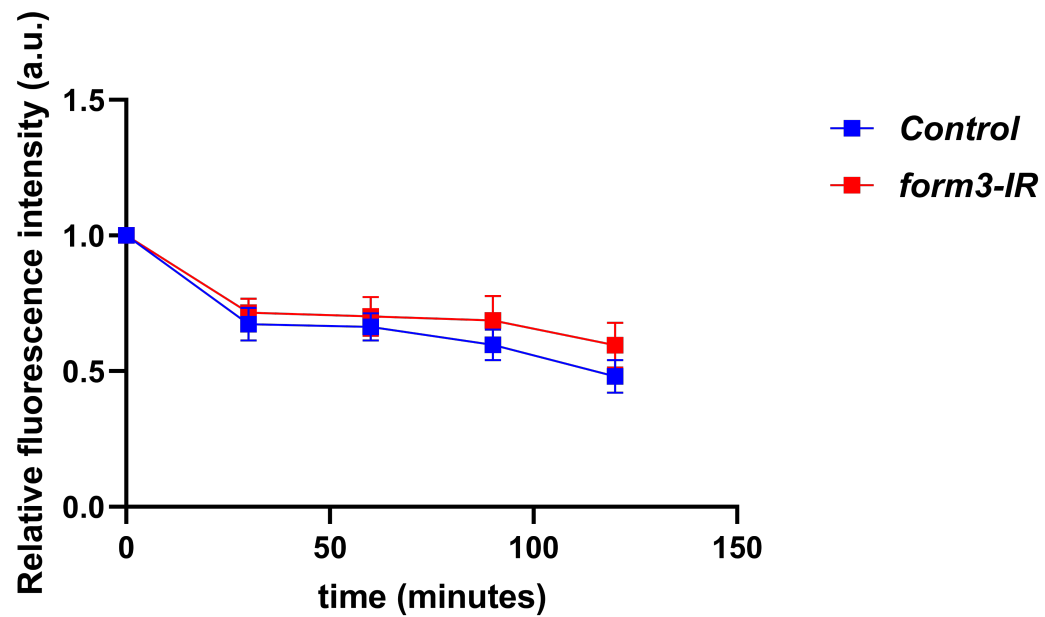


Fig. S5. *form3* does not affect MT turnover rate for the subpopulation of MTs that remain in *form3*-depleted CIV neurons. Quantitation of time-lapse imaging of MT stability over 120 minutes (see also Figure 5C-F). Statistical test performed: Unpaired t-test at 0, 60, and 120 minutes, not significant $p > 0.05$. Error bars indicate SEM.

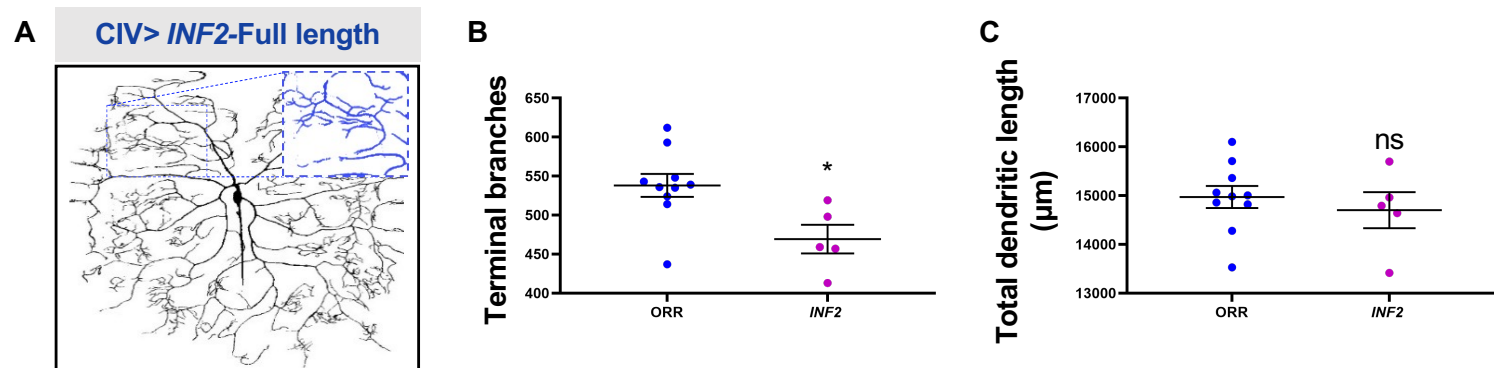
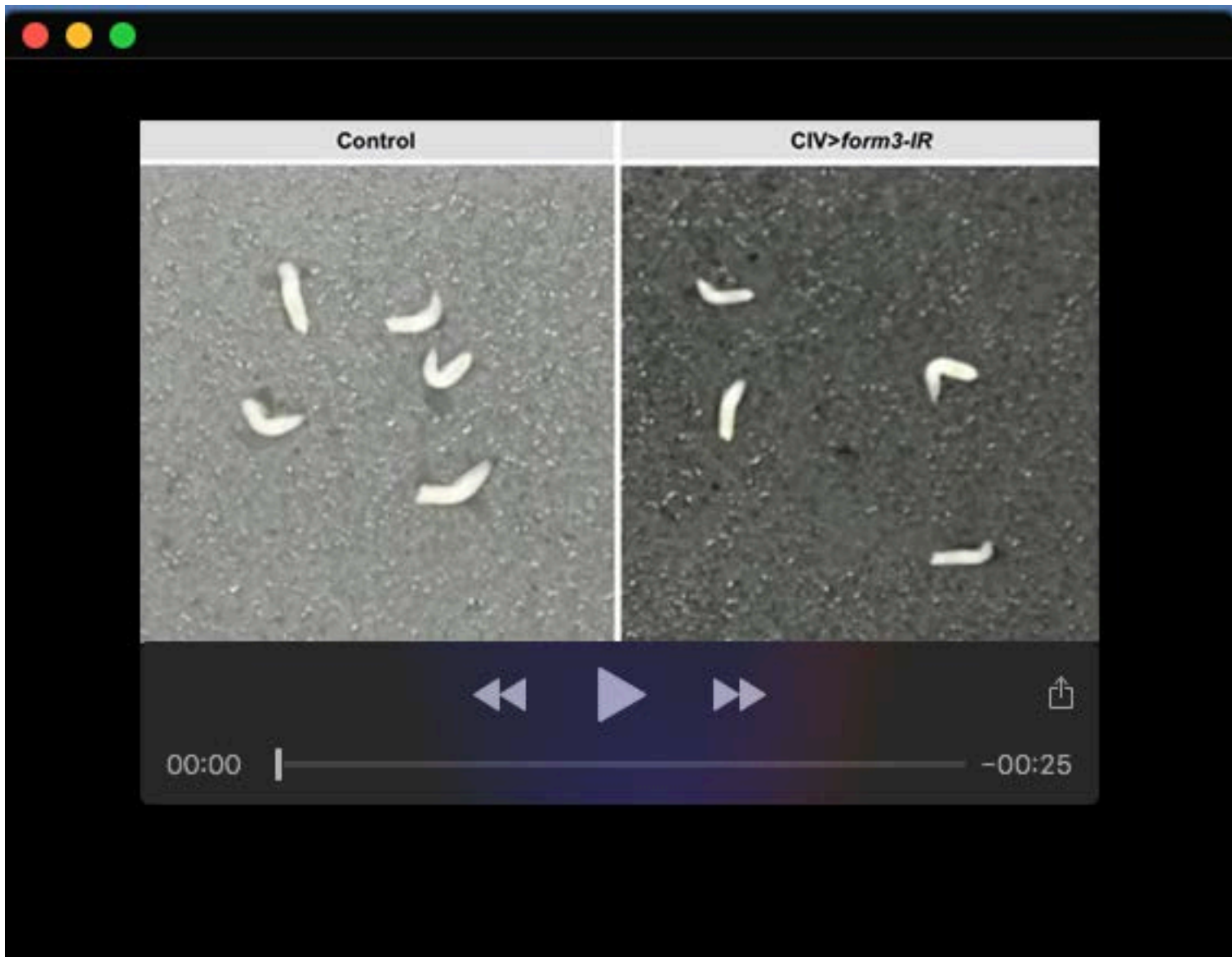
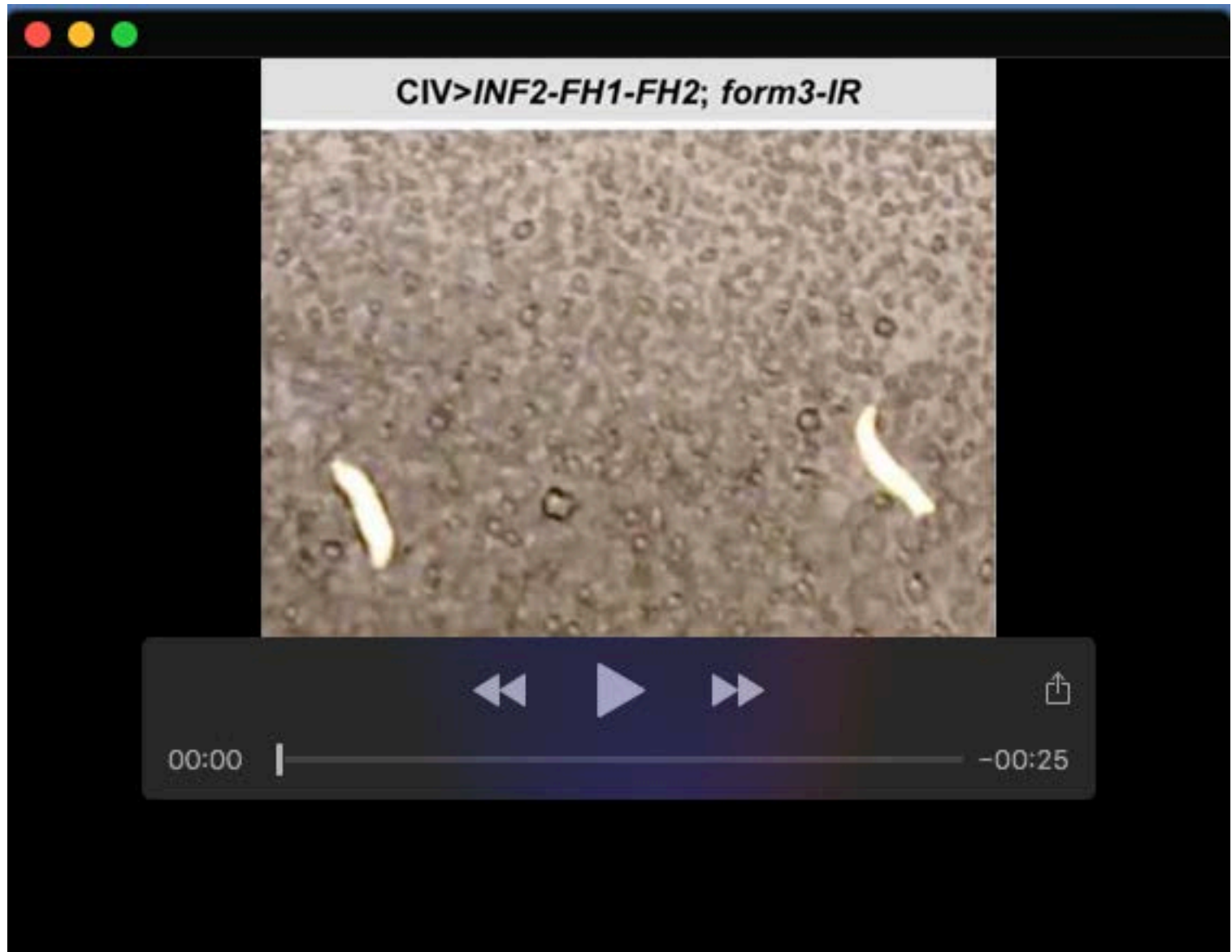


Fig. S6. Quantitative analysis of *INF2* full length and *INF2*-FH1-FH2 overexpression on dendritic morphology. (A) Representative image of CIV-specific expression of full length *INF2*. (B,C) Quantitative analyses of the terminal branches and total dendritic length of control (N=10) and *INF2* (N=5). Statistical test performed: (B) unpaired t-test, $p=0.0152$; (C) unpaired t-test, ns represents not significant $p>0.05$.



Movie 1: form3 disruption in CIV nociceptive neurons severely impairs heat-evoked rolling behavior.



Movie 2. INF2-FH1-FH2 rescue of form3 impaired heat-evoked nociceptive rolling behavior.

Supplemental Materials and Methods

Synthetic Form3-RNAi resistant coding sequence (FLAG tag @C-terminus)- corresponding to Form3-PA isoform

Start Methionine

Codon modified 54bp sequence highlighted in yellow, with native nucleotides marked in red and silent mutation nucleotides marked in blue

```
atgactcacgcatcggcctggactacattgtcgcgagaatcgtgactacattgctaagctg
M D S R I G L D Y I V E N R D Y I A K L
ggcgctgccctggacaccagaatgccaccgtcaagaagcaggtcttcgagctcctctcc
G A A L D T Q N A T V K K Q V F E L L S
gcgctgtgcgacctacagccccgatggatattgcacgagccatcgaaaccctagaattttac
A L C A Y S P D G Y A R A I E T L E F Y
aagaatctgaaaaacaacgctatcgttttaaaatcgtgattaatgagttggaattgagc
K N L K K Q R Y R F K I V I N E L E L S
agtgccgctgcccatccgcccctggactaccaggccgcccctgctggccttcatcaactgt
S A A A H P P L D Y Q A A L L A F I N C
gtcatcatctcggcggccactctacaggagcggattcgcattcgcacgaatttataggt
V I I S A A T L Q E R I R I R N E F I G
ctcaaagttttgccgctgctcaataacctaaagaaagtcgcacaaagtggtgggcatatc
L K V L P L L N N L R K V A Q S V G D I
attgtacaattggacgtattcgtggagcagcaggaatgcgacgaggcccagagccttccag
I V Q L D V F V E Q Q E C D E A Q S L Q
gcgcccgatggcatcaatctcaactcgcattcttgatgtcttctacgccattttgagacag
A P D G I N L N S H L D V F Y A I L R Q
gtggctgatacgccacaggaagtgccattcctcaacatactgcagcacctgctgcgcatc
V A D T P Q E V P F L N I L Q H L L R I
gatcccaaggagccgctcagcgacatcatctgggacaccacagagcgtctggtccaccgc
D P K E P L S D I I W D T T E R L V H R
gccacgctcctcgaaagtcacgaggattcagtgcgccctgctgcgcacgcccagtagccag
A T L L E S H E D S V R L L R T P S S Q
aagttcgcctgccagagttgtcgcggcagcgatgccagcagccccaccgcaagccctct
K F A C Q S C R G S D A S S P T R K P S
cagccggtgggctgtcggccaagacgacgcctccaccacccccaccacccatggcacc
Q P V G V S A K T T P P P P P P P P M A P
gcagcaccaccgctccgcccaccgcccagataaatggggcagcaccgcccaccaccgccc
A A P P P P P P P I N G A A P P P P P P
ccatgatcaatggtggcgcattgcctccgcccaccaccgcccctctatgcaaatggcc
P M I N G G A L P P P P P P P S M Q M A
tcacggcccaggacaccagatcccttggcagcggaggcgggtggccactgccatactgctg
S R P R T P D P L A A E A V A T A I L L
ccgcaacaggacacaccgctcccaaggccaagatgaagaccattaactggggcaagata
P Q Q D T P A P K A K M K T I N W G K I
ccgcacaacaaggtcctgggcaagcagaacatctggagattgtggccagcaatcaccag
```

P H N K V L G K Q N I W S I V A S N H Q
gacagcccgatgcaggacatcgactggaacgagatggagggactcttctgcctgcaaaca
D S P M Q D I D W N E M E G L F C L Q T
gccagtgcgcagggatcaccaagttgggacgggatggcagtcaggccgcccggatcc
A S A Q G S P K L G R D G S Q A A A G S
aatggctgcgataccctggaccgaaagtccaaaaaggagagcacagagatcacctgctt
N G C D T L D R K S K K E S T E I T L L
gacggcaagcgaagtctgaatgtgaatatcttcctgaagcaattccgcaccagcaacgac
D G K R S L N V N I F L K Q F R T S N D
gacatcatccagttgatccggcagggagcccacgaggagatcggagcggagagattgagg
D I I Q L I R Q G A H E E I G A E R L R
ggtttgctgaagataatgcccgaggtggatgagctggacatgctgaagggattcaacggg
G L L K I M P E V D E L D M L K G F N G
gataaggcacgactgggcaatgccgagaagttcctgctgcagctgctcgaggtgcccaat
D K A R L G N A E K F L L Q L L E V P N
tacaattgcggatcgagagcatggtgctcaaggaggagtttgccggaatgtggcctat
Y K L R I E S M L L K E E F A A N V A Y
ctggagccctgtatcaattctatgctctatgctggcgacgatctactgaataataagact
L E P C I N S M L Y A G D D L L N N K T
cttcaggaggtcctttacatggtcgttggtggctggaaatttccttaactccggcggctat
L Q E V L Y M V V V A G N F L N S G G Y
gcaggaaatgcggcggcgctgaagctatcatcgctgcaaaagctaactgatatccgggcg
A G N A A G V K L S S L Q K L T D I R A
aataagccgggcatgaacctcattcacttcgtggctcttcaggcggagaaacgcaatccc
N K P G M N L I H F V A L Q A E K R N P
gaactgcttcaattcacaggacaactgagcaacctcgaaagtgccagcaaaacaacatca
E L L Q F T G Q L S N L E S A S K T T S
gagcagatcaacaatgaaatcaacacactggacggcaggatcagaagaatagccagacag
E Q I N N E I N T L D G R I R R I A R Q
atcgaacaacctgccacggatgtggacatcaaggagcaaatggccgactttttgcaggcc
I E Q P A T D V D I K E Q M A D F L Q A
gccgaatccgagctatccgtcctccaagctggcatgaaacaagtggagtcaatgcggctc
A E S E L S V L Q A G M K Q V E S M R L
aaaatgtccgagttcttctgcgacgatgcggccaccttcgggctggaggagtgttcaag
K M S E F F C D D A A T F R L E E C F K
atcttcacaatttctgtgataaattcaagcaggcgggtcaaggagaacgagcgcgccag
I F H N F C D K F K Q A V K E N E R R Q
cagcaggagcaacaggccacgcttaggaggaagcagcgcgaggagcagctggcccgcaga
Q Q E Q Q A T L R R K Q R E E Q L A R R
gccagacagattggtcaggctggaacgccagtttcggactcggagcattccttcttgggc
A R Q I G Q A G T P V S D S E H S F L G
gatgctatcttcgatcctagggttagtccggcgtgagtcgccgccacctgggatccgga
D A I F D P R A S P A L S R R H L G S G
gagatcagcaatggtttcatccgcctggaacaagacggagccttccggacatcacacc
E I S N G F I R L E Q D G A S P D I T P
aacggaagtctgaggcgtcggcgtagtcgagttcttgccgaggaggatgacctgatggag
N G S L R R R R S R V L A E E D D L M E
ttccttcggagttcgacgggtcctcaccacgatggacacaatagcagggagcgggaaggcg

F L R S S T G P H H D G H N S R E R K A
gcctacggcagcttggatcgctcgtgggctcgtcgtgcccgctccggaagttccagtcgc
A Y G S L D R S W A R R A R S G S S S R
aaacgacccgatttgcacattgactttggcatggatcgtgaacgggcccagctccccg
K R P D L L N I D F G M D R E R A S S P
gctcctcttcttcagcagcagcagcaaaatgtccaggagcagactgcaatctccattggcc
A P L L Q Q Q Q Q N V Q E R L Q S P L A
agtacagctggaacgccacaacggcagcgaatacgcccacgggagtgatcggcgatt
S T A G T P T T A A N T P T G S G S A I
gctcagacgccatctaataacgaggatgcaaaacgaagaatcccgtgagtgccgcccag
A Q T P S N N E D A K P R I S R E W R Q
aagatcgagacgtggcttcaatccaacgagagcagatgagaagcaaaacgaggagtagcag
K I E T W L Q S N E S D E K Q N E E Y R
cggaagcgtcgtcgttcaacgccaataggcagatcgctcgaaaacgaaactgaaaacgaa
R K R R L V N A N R R S L E N E T E N E
cgaaaactggacccttgccggaggagaagatcctgccttcgacgacgacagctacgcca
R K L D P L P E E K I L P S T T T A T P
acgaatacgctacgaccacgaatcccactaactccactaatagaatggatcaggagtc
T N T P T T T N P T N S T N R M D Q E S
ggcaaatatcagcgcgtctatgccgactggaagccctcgaggacgctggagcagacggac
G K Y Q R V Y A D W K P S R T L E Q T D
gtggtggccaatctgcaggccattgccgatgccagccgacgatgcattgcgtcaacat
V V A N L Q A I A D A Q P H D A L R Q H
cgccgacagcagatcgcaggaacagccgagtcctcatagcacttcaatcgatagccgaggag
R R Q R S Q E Q P S P I A L Q S I A E E
gatcgtcgaaagtcccttattcagaaacaggggtgaaagggacaagagcaacgagcggttg
D R R K S L I Q K Q G E R D K S N E R L
caaatctatatcaggcagatcctccagccgggaactgcagcctgcgaaaacggaggagcat
Q I Y I R R S S S R E L Q P A K T E E H
ccactgccaccaagtcaccaagccacaagtgccgacgacacctttgccagcctgctc
P L P P K S P K P Q V S D D T F A S L L
agtcaccacaagacccaaaacgagatgcagggtcctccaaggacgtggatgcggataat
S H H K T Q N E M Q G S S K D V D A D N
atagagacgccaccagtgagccgacgggtcatagccacgcccaccaccacagtggtcagc
I E T P P V S R R V I A T P T T T V V T
gtgagcatgacggataaaccaaggctgcgacggaggagaagatcaaccagcggaaacag
V S M T D K P K A A T E E K I N P A E Q
gatgcgcccgggtcacttcgatcgccatgccctggctcgccgcacacgacgctacaaaaga
D A P G H F D R H A L A R R T R R Y K R
cccacggactacagcagtggaatgaggaggcgtgaccaccagcacagcagaggcaaag
P T D Y S S G N E E A L T T S T A E A K
acttctccatcgaagccagagccacccgacccgagaagtccaagcagaaggagcgcagc
T S P S K P E P P A P E K S K Q K E R T
atcaacaagctggagaaggtgggtcgccacataagctccatcaatcaggaggatgtaagg
I N K L E K V G R H I S S I N Q E D V R
gaggccattcggaatcttaaatcacccaggggaactccagaacgaccttgagtcgcca
E A I R N L K S P T G T P E R P W S P P
cgggatatacacaccctccaagctaaaactgtccgcccagtggtcaccacgaactgaatgac

R D I T P S K L K L S A S G H H E L N D
gaaggcttcgaggagactcagagtcttgtgtcggacactccgtctcacgaaagggcgag
E G F E E T Q S L V S D T P S H G K G E
agcacaactcctcctgcaacgaggggtgtaaacgagactcctgcccggcagcggccgatg
S T N S S C N E G V N E T P A R Q R P M
cagaagcaaaagcccacaaccaccagcatcagccagatgggcagtcgggtggccgatcgc
Q K Q K P T T T S I S Q M G S R L A D R
ctgcagcaggccaggatgaagagttccggatcctcaggatcggcagccagcaagtcacaa
L Q Q A R M K S S G S S G S A A S K S Q
aaccaaatccctgccacccaaactgcaacggtcaagaggagcctctccgccagcagaccg
N Q I P A T Q T A T V K R S L S A S R P
ctgcgcatgcccaacggtcagccggtggccagtcgagctccgctgagatccgcatccact
L R M P N G Q P L A S A A P L R S A S T
gtgagacgctcgcgcaggagcaacaggttctagccggcgtggagcggagcagttcgaga
V R R S P Q E Q Q V L A G V E R S S S R
aacagtctgcgctcctcgcgatcgtccatcaacagtgaggcctccactcaaactgtagtg
N S L R S S R S S I N S G A S T Q T V V
agacgactgcccgcggtcagcagcgggagccactgtgtccggtgactcctcgcccagc
R R L P A V Q R A G A T V S V D S S P S
aaaagaccactggccgcccagaatctgcgacctaccagggacgtggagtccccgccagc
K R P L A A Q N L R P T Q G R G V P A S
aggagcagcagtagcgggtcgagtggtgggacccagtgatccttggtgcgagcaagatg
R S S S S G S S V G P S V I L V R S K M
tccaacacggctccgaaatcgagtatccatggttagcaccagttttaaggaaaaccagtcc
S N T A P K S S I H G S T S F K E N Q S
cagtcccaacccccagtcacagtcaccgaatgagcgcgctcgcagcgtggtgctggtgaaa
Q S Q P Q S Q S R M S A A R S V V L V K
aatgccctgaaccagcagcagcaggccaggatgagtgccaacccccagtcgcgagcagagg
N A L N Q Q Q Q A R M S A N P S P Q Q R
agcactagcagcagtcgatccgtgagcagcttcatgcgacccacggccagcagtgccacc
S T S S S R S V S S F M R P T A S S A T
aagcgacagaaggactacaagacgatgacgacaagtga
K R Q K D Y K D D D D K -